

## Article

# Cyclic evolution of phytoplankton forced by changes in tropical seasonality

<https://doi.org/10.1038/s41586-021-04195-7>

Received: 30 October 2020

Accepted: 29 October 2021

Published online: 1 December 2021

 Check for updates

Luc Beaufort<sup>1</sup>✉, Clara T. Bolton<sup>1</sup>✉, Anta-Clarisso Sarr<sup>1</sup>, Baptiste Suchéras-Marx<sup>1</sup>, Yair Rosenthal<sup>2</sup>, Yannick Donnadieu<sup>1</sup>, Nicolas Barbarin<sup>1,3</sup>, Samantha Bova<sup>2,4</sup>, Pauline Cornuault<sup>1,5</sup>, Yves Gally<sup>1</sup>, Emmeline Gray<sup>1,6</sup>, Jean-Charles Mazur<sup>1</sup> & Martin Tétard<sup>1</sup>

Although the role of Earth's orbital variations in driving global climate cycles has long been recognized, their effect on evolution is hitherto unknown. The fossil remains of coccolithophores, a key calcifying phytoplankton group, enable a detailed assessment of the effect of cyclic orbital-scale climate changes on evolution because of their abundance in marine sediments and the preservation of their morphological adaptation to the changing environment<sup>1,2</sup>. Evolutionary genetic analyses have linked broad changes in Pleistocene fossil coccolith morphology to species radiation events<sup>3</sup>. Here, using high-resolution coccolith data, we show that during the last 2.8 million years the morphological evolution of coccolithophores was forced by Earth's orbital eccentricity with rhythms of around 100,000 years and 405,000 years—a distinct spectral signature to that of coeval global climate cycles<sup>4</sup>. Simulations with an Earth System Model<sup>5</sup> coupled with an ocean biogeochemical model<sup>6</sup> show a strong eccentricity modulation of the seasonal cycle, which we suggest directly affects the diversity of ecological niches that occur over the annual cycle in the tropical ocean. Reduced seasonality in surface ocean conditions favours species with mid-size coccoliths, increasing coccolith carbonate export and burial; whereas enhanced seasonality favours a larger range of coccolith sizes and reduced carbonate export. We posit that eccentricity pacing of phytoplankton evolution contributed to the strong 405,000-year cyclicity that is seen in global carbon cycle records.

Coccolithophores precipitate half of the biogenic CaCO<sub>3</sub> that is exported from the open ocean<sup>7</sup> and their fossil platelets (coccoliths) first appeared in sediments during the Upper Triassic, around 215 million years ago (Ma). Thereafter, coccolithophores rose to dominance<sup>8</sup> and became a key biological modulator of the global carbon cycle through photosynthesis and calcification<sup>9</sup>. In the dominant Cenozoic Noelaerhabdaceae family (including *Emiliania huxleyi* and *Gephyrocapsa*), species are defined by the morphological characteristics of their coccoliths, with size being a key criterion<sup>10</sup> that is related to cell size<sup>11</sup>. For *Gephyrocapsa* and *Emiliania*, phylogenies reconstructed from gene sequences indicate that morphology-based definitions correspond to biological species<sup>3,12</sup>. Within a given Noelaerhabdaceae population—which is typically dominated by one species but includes several—interspecific and intraspecific changes in coccolith length and mass occur in response to environmental parameters such as carbonate chemistry<sup>1</sup> and temperature<sup>2</sup>. Studies of coccolithophore evolution have focused on geological-timescale changes in species richness and turnover<sup>13</sup>, coccolith carbonate accumulation<sup>8,14</sup> or calcification potentially driven by carbon cycle changes<sup>15</sup>. In addition, climate changes induced by orbital cycles (on timescales of tens to hundreds of thousands of years) strongly influence the composition of nannofossil assemblages<sup>16–18</sup>. However, so far the effects of orbital cycles

on coccolithophore evolution, coccolith morphology and carbonate production have not to our knowledge been examined simultaneously.

Here we quantify the Pleistocene history of tropical Noelaerhabdaceae evolution at high resolution (around two thousand years, kyr), using coccoliths preserved in nine well-dated sedimentary sections from the Indian and Pacific Oceans cored during International Ocean Discovery Program (IODP) and International Marine Past Global Changes Study (IMAGES) expeditions (Extended Data Table 1). We use artificial intelligence microscopy to create a biometric database of over 7 million coccoliths from more than 8,000 samples (Methods). The strong similarity of morphometric patterns observed at each site (Extended Data Fig. 1) led us to build composite frequency contour plots of coccolith size and mass, representing larger-scale evolutionary change (Fig. 1a, Methods). Patches denoting high frequency of a particular size correspond in many cases to described acmes of Noelaerhabdaceae species<sup>19–21</sup> or proposed evolutionary events<sup>3</sup> (Fig. 1). The most recent evolutive phase, which started around 550 thousand years ago (ka), is attributed to a radiation event and the emergence of new *Gephyrocapsa* species, on the basis of a genetic study of extant taxa and its temporal correlation to low-resolution coccolith morphometric data<sup>3</sup>. Over the Pleistocene, average coccolith size shows an increase that corresponds to a gradual shift in dominance from smaller

<sup>1</sup>Aix-Marseille University, CNRS, IRD, INRAE, CEREGE, Aix-en-Provence, France. <sup>2</sup>Department of Marine and Coastal Sciences, and Earth and Planetary Sciences, Rutgers, State University of New Jersey, New Brunswick, NJ, USA. <sup>3</sup>Present address: TOTAL S.A., Pau, France. <sup>4</sup>Present address: Department of Geological Sciences, San Diego State University, San Diego, CA, USA. <sup>5</sup>Present address: MARUM, Universität Bremen, Bremen, Germany. <sup>6</sup>Present address: The Open University, Milton Keynes, UK. ✉e-mail: beaufort@cerege.fr; bolton@cerege.fr

# Article

to larger coccoliths (Fig. 1b). On orbital timescales, global ice volume and deep-sea temperature as represented by benthic foraminiferal  $\delta^{18}\text{O}$  show a dominance of 41-kyr and later around 100-kyr glacial–interglacial cycles<sup>22</sup> (Fig. 1c). By contrast, average coccolith length follows a regular cycle that is highly coherent (greater than 99.9%) with the orbital eccentricity periods of 405 kyr (e405) and of 124 and 95 kyr (e100)<sup>23</sup> (Extended Data Fig. 2a), with larger average size occurring at high eccentricity with a slight time lag (Fig. 1b).

Average size or mass of coccoliths in a Noelaerhabdaceae population may vary because of macro- and/or microevolution, or because ecological changes modulate the relative abundances of species in different size ranges. To build a metric that describes only species evolution, we remove the effect of relative abundance changes related to ecology<sup>24</sup> by formulating a morphological divergence index (MDI), calculated as the difference in average coccolith mass between two size classes—larger and smaller than 3  $\mu\text{m}$  (Methods). Thus, MDI quantifies morphological divergences of species over time through evolution, and could be driven by changes in size or degree of calcification (see Fig. 2 for a conceptual explanation). Noelaerhabdaceae coccolithophores spread rapidly throughout the oceans and are often cosmopolitan, resulting in the same species being present in many regions, but with different relative abundances<sup>12,19</sup>. MDI varies independently of regional ecological specificities, and MDI records from sites in distinct oceanographic biomes<sup>25</sup> and climatic regimes (for example, warm pool, monsoon-dominated; Extended Data Table 1) are highly intercorrelated, all showing significant e405 and e100 periods (Extended Data Figs. 1, 2). Therefore, we produce a composite MDI stack, which preserves the high resolution of each dataset (Fig. 1e, Methods). The MDI stack, interpreted as reflecting evolutionary changes in morphological diversity, shows strong 405-kyr pacing throughout the Pleistocene irrespective of glacial–interglacial background state. Cross-spectral analysis indicates significant (greater than 90%) coherency between the stack and Earth’s eccentricity periods since 2.8 Ma (Fig. 1d). This pattern cannot be the result of differential dissolution on coccolith morphology (Methods) and in contrast to MDI, Pleistocene deep-sea  $\text{CaCO}_3$  dissolution generally follows glacial–interglacial cycles<sup>26</sup>. Similarly, coccolith morphological evolution appears not to be responding directly to physical parameters covarying with global ice volume, such as sea level or ocean temperature. Although eccentricity forcing on coccolithophore productivity has previously been suggested<sup>27,28</sup>, our new dataset reveals that eccentricity cycles instead forced the evolution of the Noelaerhabdaceae.

Cyclic coccolithophore evolution may have affected the ocean carbon cycle through coccolith carbonate production and burial in sediments<sup>14,29</sup>. Coccolithophores produce large amounts of calcite during blooms<sup>27,30</sup>, and sediments are often dominated by a few opportunistic species, for example *E. huxleyi* (0–90 ka)<sup>19</sup> and *Gephyrocapsa caribeanica* (280–570 ka)<sup>20</sup> in the late Pleistocene. We estimate the mass accumulation rate of Noelaerhabdaceae coccoliths (NoMAR) in our cores and produce a stacked record (Fig. 1g, Methods). Noelaerhabdaceae coccoliths represent on average half of the total calcareous nanoplankton mass in our studied cores (Extended Data Table 2). The two components of NoMAR, coccolith flux and average mass, are separated in Extended Data Fig. 3. This reveals that NoMAR is primarily driven by changes in coccolith flux, and that flux and mass often have opposing effects on NoMAR as medium-sized, lighter species (for example, *E. huxleyi* and *G. caribbeanica*) contribute the most to coccolith carbonate export. Thus, higher NoMARS when mid-size opportunistic species dominate often correspond to lower MDI values (Fig. 1e, g). The dominance of these opportunistic species coupled with high coccolithophore accumulation in sediments during eccentricity minima is also recorded in the extra-tropics<sup>27</sup>. In contrast to MDI, local ecological conditions affecting productivity and export—and possibly water depth affecting coccolith accumulation—also influence NoMAR, so a linear relationship between the two is not expected. Although it is impossible to quantify the relative effects of these factors, common trends between

sites emerge despite different absolute values and these are reflected in the NoMAR stack. Thus, NoMAR combines global evolutionary and local ecological drivers of calcite production, whereas MDI should exclusively record evolution. Nevertheless, the NoMAR composite record shows strong eccentricity periodicities that are significantly coherent with MDI throughout the Pleistocene (Fig. 1f), showing a strong imprint of coccolithophore morphological evolution on carbonate production and burial.

## MDI and long-term seasonal variations

We hypothesize that the MDI index responds to variations in the amplitude of tropical seasonality. In low latitudes, seasonal contrast is related to the eccentricity of Earth’s orbit<sup>23,31</sup> both directly, because the ellipticity of the orbit determines the distance between the Sun and the Earth during each season, affecting radiation intensity, and indirectly, because eccentricity modulates the effect of precession on seasonal insolation contrast. Seasonal contrast is greater during periods of high eccentricity. To our knowledge, the eccentricity-paced rhythm of surface-ocean seasonality that dominates MDI has not been documented previously because most proxies record integrated annual average conditions or a specific season. In the modern intertropical ocean, large seasonal changes in the properties of the upper water column (for example, mixed-layer depth and nutrient availability) are associated with the seasonally reversing monsoon systems and latitudinal migrations in the intertropical convergence zone. The seasonal succession of coccolithophore species, a characteristic of phytoplankton ecology, is indicative of their adaptation to the different ecological niches created by seasons<sup>24</sup>. In the modern ocean, the highest phytoplankton diversity is found in the tropical band, a pattern probably related to high temperatures and stable conditions, whereas seasonal species turnover is highest at mid-latitudes because of a strong seasonal temperature contrast<sup>32</sup>. Intra-annual dynamics of net primary production (NPP) are good descriptors of the range of oceanographic niches and biomes<sup>25</sup>, because NPP represents the integrated biological response to all of the changes forced by the ocean–atmosphere coupled system. To demonstrate the effect of orbital configuration on NPP seasonality and therefore niche availability, we simulated monthly oceanic NPP using the fully coupled IPSL-CM5A2 model<sup>5</sup>, which includes the ocean biogeochemistry model PISCES-v2<sup>6</sup>, for seven early Pleistocene time intervals that cover a large eccentricity spectrum with different precession conditions but with similar ice volume and obliquity (Extended Data Table 3, Fig. 1b). The results of these simulations for the tropical Indian and western Pacific Oceans show that the seasonal range of NPP increases with eccentricity, a trend that parallels the eccentricity sorted values of MDI in our Plio-Pleistocene time series (Fig. 3).

In the simulations, the increase in amplitude of the NPP seasonal cycle (Fig. 3a, Extended Data Fig. 4a–e) is primarily driven by higher productivity during boreal summer, especially in the eastern Indian ocean. This increase is forced by the modification of atmosphere–ocean dynamics in response to variations in the amplitude and seasonality of insolation forcing (Extended Data Fig. 5a–c). Eccentricity acts on sea-level pressure over continental Asia (Extended Data Fig. 5d–h) through insolation, inducing modifications of sea-level pressure gradients and low-level wind circulation over the Indo-Pacific Warm Pool (IPWP) (Extended Data Fig. 4f–h). Changes in atmospheric dynamics are responsible for regional and seasonal enhancement of NPP at high eccentricity (Extended Data Fig. 4a–c), either through the generation of anomalous upwelling along the equator (southwest of India) or the modification of the hydrological cycle that create more favourable conditions for intense vertical mixing (Extended Data Fig. 6a, c), depending on precession. Overall, those localized increases in the amplitude of the seasonal cycle lead to a less homogeneous upper ocean in the IPWP region at high eccentricity (Fig. 3a, Extended Data Fig. 4a–c). We propose that during times of high eccentricity, the higher seasonal

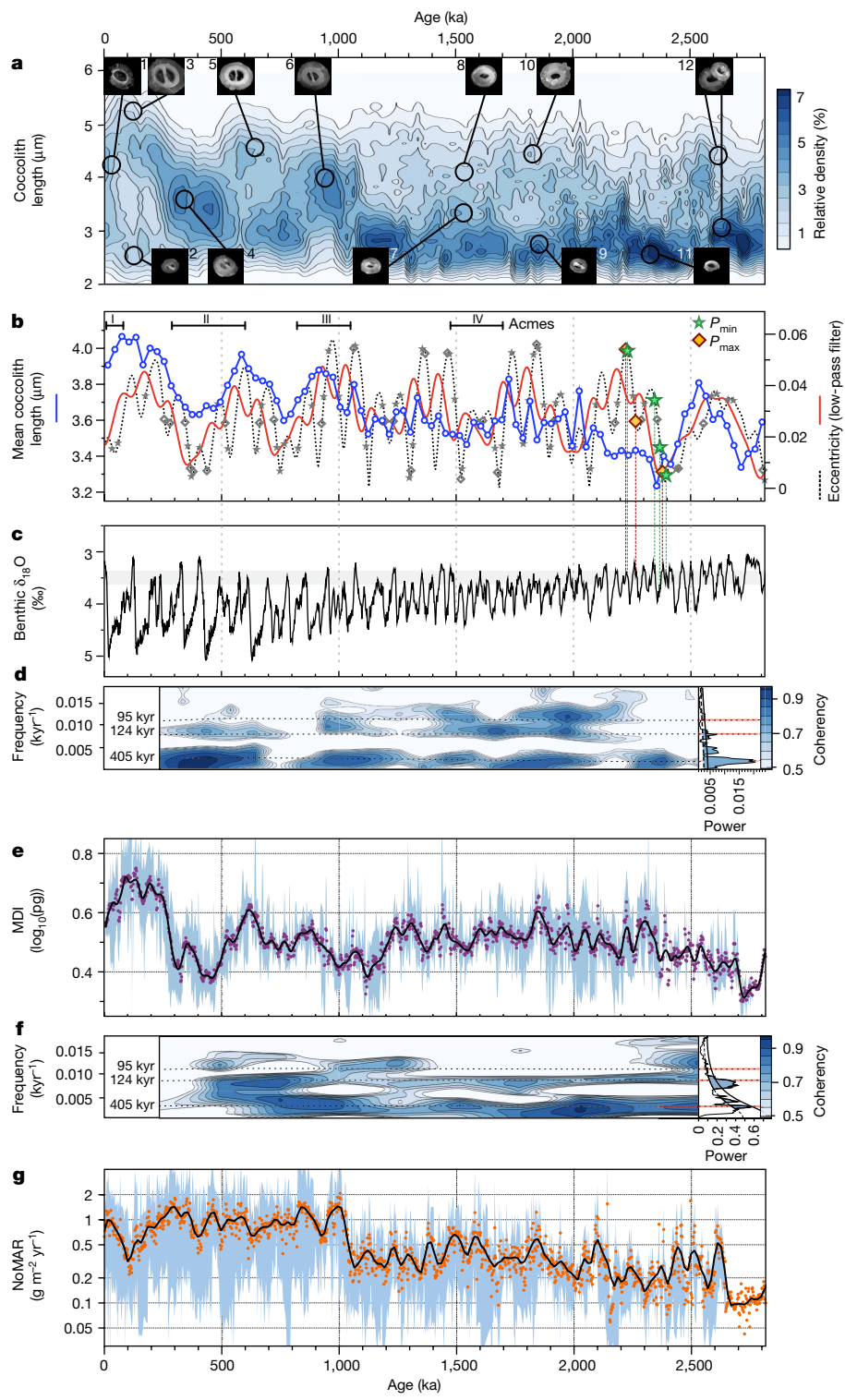


**Fig. 1 | Noelaerhabdaceae coccolith morphology and accumulation, eccentricity, and climate over the last 2.8 million years.** **a**, Frequency contour plot of multi-site stacked coccolith length (Methods). Scanning electron microscope images represent examples of the diversity of Noelaerhabdaceae morphologies over time. 1, *Emiliania huxleyi*; 2, *Gephyrocapsa ericsonii*; 3, *Gephyrocapsa oceanica*; 4, *Gephyrocapsa caribbeana*; 5–6, *Gephyrocapsa omega*; 7–8, mid-size *Gephyrocapsa*; 9, small *Gephyrocapsa*; 10, *Pseudemiliania ovata*; 11, *Reticulofenestra minuta*; 12, left: *P. ovata*, right: *R. minutula*. **b**, Mean coccolith length in the stack (blue), plotted with Earth's eccentricity<sup>23</sup> (dotted black line) and low-pass-filtered eccentricity with an angular frequency of  $0.021 \text{ kyr}^{-1}$  (red). Described Noelaerhabdaceae acmes<sup>19–21</sup> are shown as black bars (I, *E. huxleyi*; II, *G. caribbeana*; III and IV, mid-size *Gephyrocapsa*). Coloured stars and diamonds on the eccentricity curve show the timing of actual orbital configurations used in model simulations ( $P_{\max}$ , precession with perihelion in December;  $P_{\min}$ , precession with perihelion in June); smaller grey symbols indicate times throughout the record with similar eccentricity and precession configurations to those modelled (Methods). **c**, LR04 benthic foraminiferal  $\delta^{18}\text{O}$  stack<sup>22</sup>. Grey band illustrates the small range of benthic  $\delta^{18}\text{O}$  between model simulations. **d**, Left, evolutive cross-spectral analysis between MDI and eccentricity (Methods). Colour-scale shows coherency (90% confidence level (CL) above 0.7); horizontal dashed lines show eccentricity periods. Right, MTM spectral analysis of detrended MDI stack. Shaded areas are above the CL90% (dashed line). Solid black line is CL95%. **e**, MDI stack (2-kyr resolution) (Methods). **f**, Left, evolutive cross-spectral analysis between NoMAR and MDI. CLs as in **d** (left). Right, MTM spectral analysis of detrended NoMAR stack. CLs as in **d** (right). **g**, NoMAR stack (2-kyr resolution; see Methods). MDI and NoMAR stacks are smoothed with a Loess function, and blue shading shows maximum and minimum values across all records.

December;  $P_{\min}$ , precession with perihelion in June); smaller grey symbols indicate times throughout the record with similar eccentricity and precession configurations to those modelled (Methods). **c**, LR04 benthic foraminiferal  $\delta^{18}\text{O}$  stack<sup>22</sup>. Grey band illustrates the small range of benthic  $\delta^{18}\text{O}$  between model simulations. **d**, Left, evolutive cross-spectral analysis between MDI and eccentricity (Methods). Colour-scale shows coherency (90% confidence level (CL) above 0.7); horizontal dashed lines show eccentricity periods. Right, MTM spectral analysis of detrended MDI stack. Shaded areas are above the CL90% (dashed line). Solid black line is CL95%. **e**, MDI stack (2-kyr resolution) (Methods). **f**, Left, evolutive cross-spectral analysis between NoMAR and MDI. CLs as in **d** (left). Right, MTM spectral analysis of detrended NoMAR stack. CLs as in **d** (right). **g**, NoMAR stack (2-kyr resolution; see Methods). MDI and NoMAR stacks are smoothed with a Loess function, and blue shading shows maximum and minimum values across all records.

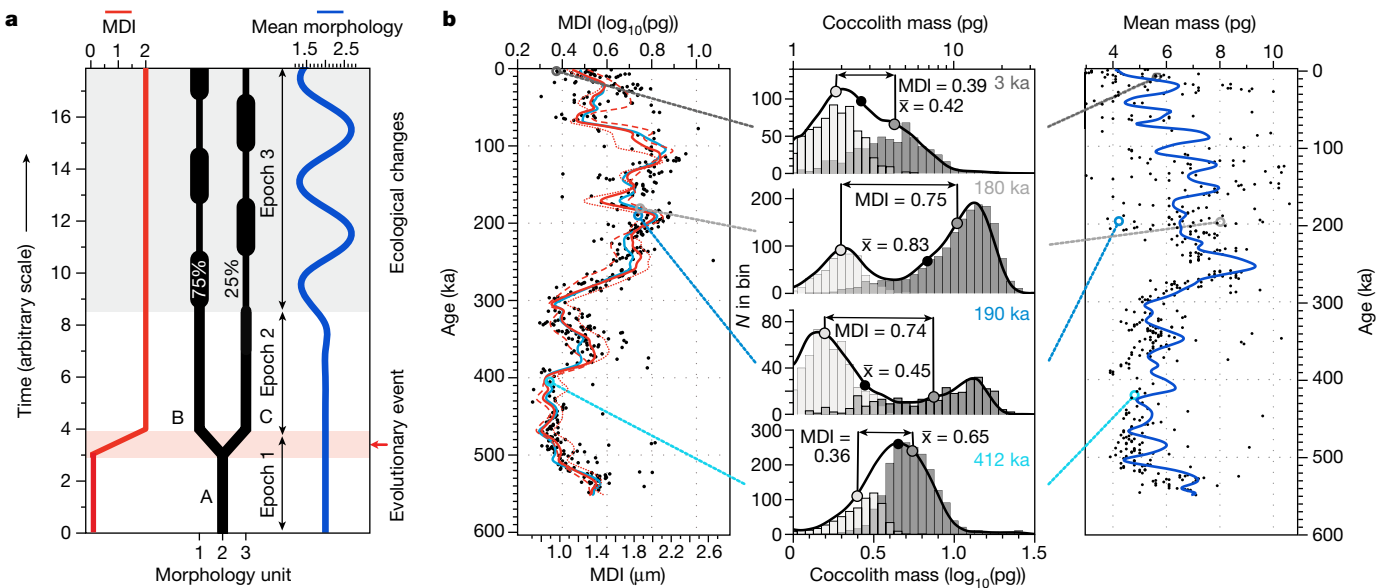


**Fig. 2 | MDI concept.** **a**, Schematic representation of MDI (conceptual model).

We consider an evolutionary sequence in which species A (intermediate morphology) evolves into species B (smaller) and C (larger). In epoch 2, B and C have equivalent proportions, and in epoch 3, they fluctuate in relative abundance between 25% and 75%. The evolutionary event between epochs 1 and 2 (red shading) is not detected in mean population morphology (for example, size, mass). In epoch 3, fluctuating ecology produces population dynamics detected in mean morphology (grey shading). With a biometric boundary of 2 units, MDI jumps from 0 to 2 from epoch 1 to 2, thus it is diagnostic of an evolutionary event. In epoch 3, MDI remains stable despite fluctuating assemblage composition. In this idealized example, average population biometry is related to ecology and MDI to evolution. **b**, MDI calculated for IODP site U1485 (example dataset). Right, average Noelaerhabdaceae coccolith mass

(smoothed using a Loess function). Middle, two size classes are created: coccoliths shorter and longer than 3  $\mu\text{m}$  (grey histograms). MDI is the difference between the average  $\log(\text{mass})$  of each class (light and dark grey dots on histograms). Thus, MDI can differ substantially from average coccolith mass (black dots on mass distribution plots), and two samples can have a similar MDI but different average mass and mass distributions (for example, 180 ka versus 190 ka), or different MDI but similar averages (for example, 3 ka versus 190 ka). In this way, MDI isolates morphological variability resulting from evolutionary changes in the number of different morphotypes present within the population. Left, MDI record (identical Loess smoothing window to that in the right panel). Smoothed curves illustrate the effect of different length or mass thresholds used to calculate MDI: solid red line, 3  $\mu\text{m}$ ; red dotted line, 2.7  $\mu\text{m}$ ; red dashed line, 3.6  $\mu\text{m}$ ; solid blue line, 3.16 pg.

range of NPP in our model simulations (representing up to 100% of mean annual NPP) is indicative of more diverse ecological niches to which coccolithophores can adapt. A greater diversity of ecological niches when seasonality is high<sup>25</sup> leads to a larger number of species because Noelaerhabdaceae adaptation is characterized by the adjustment of coccolith size and degree of calcification to thrive in the new environments<sup>1,2</sup>.

### Eccentricity lag, origination and dominance

Coccolith morphological diversity clearly responds to eccentricity (Fig. 1); however, in stark contrast to Plio-Pleistocene climate proxy records<sup>22,33</sup> and coccolithophore assemblage dynamics<sup>16–18</sup>, precession and obliquity cycles are absent from the 2-kyr resolution MDI records (Extended Data Fig. 2c–k). These cycles could have been smoothed out by the evolutionary process acting as a low-pass filter, providing an explanation for the phase lag observed between eccentricity and Noelaerhabdaceae morphology (Fig. 1b, Extended Data Fig. 2a, b). We know that speciation events spread rapidly throughout the oceans<sup>12,19,21</sup>, and species dominance takes longer, as exemplified by *E. huxleyi*. This species appeared at 290 ka but did not become dominant until 90 ka<sup>19</sup>, during an intense low-eccentricity interval two e100 cycles later, when it gained a competitive advantage over *Gephyrocapsa oceanica* and *Gephyrocapsa ericsonii* (Extended Data Fig. 7). The delay between species appearance and dominance could therefore be intrinsic in smoothing out variability at precession and obliquity timescales in the MDI record (Fig. 1b, Extended Data Fig. 7). At present, the lack of precise ages for the first occurrences of Noelaerhabdaceae species in the fossil record precludes us from testing this hypothesis further.

The eccentricity lags and transfer of spectral power from high to low frequencies described here are analogous to modelling results in a previous study of deep-time carbon cycle variations on orbital timescales<sup>34</sup>, hinting that coccolithophores may drive—rather than just respond to—carbon cycle changes.

### Coccolithophores and the global carbon cycle

The persistence of e100 and e405 cycles in Cenozoic and Mesozoic records of the ocean carbon cycle (for example, per cent  $\text{CaCO}_3$  and foraminiferal  $\delta^{13}\text{C}$ ), independent of glacial–interglacial climate state, attests to the importance of biogeochemical processes operating at these timescales throughout Earth's history<sup>35,36</sup>. During the Pleistocene, Mediterranean surface  $\delta^{13}\text{C}$  records document e405 cycles more faithfully than do deep open-ocean records, suggesting a low-latitude climatic origin of this signal<sup>28</sup>. Chemical weathering has been suggested as a potential modulator of the ocean carbon cycle on 400-kyr timescales<sup>37</sup>. Similar to our coccolith records, a notable phase lag between  $\delta^{13}\text{C}$  and eccentricity is observed in the e405 band, which has been explained by the long residence time of carbon in the oceans and resultant transfer of energy from precession into eccentricity bands through a non-linear process<sup>34,35</sup>. Previous coccolith records spanning up to around 1 million years (Myr) have linked coccolithophore production to eccentricity forcing<sup>17,27</sup>. Yet changes reconstructed at our low-latitude sites cannot be explained by the hypothesis that eccentricity-driven changes in growing season length are responsible for the approximately 400-kyr cycle in coccolithophore production<sup>27</sup>. Our data and model results support the alternative hypothesis that changes in seasonality caused by the eccentricity of the Earth's orbit paced tropical

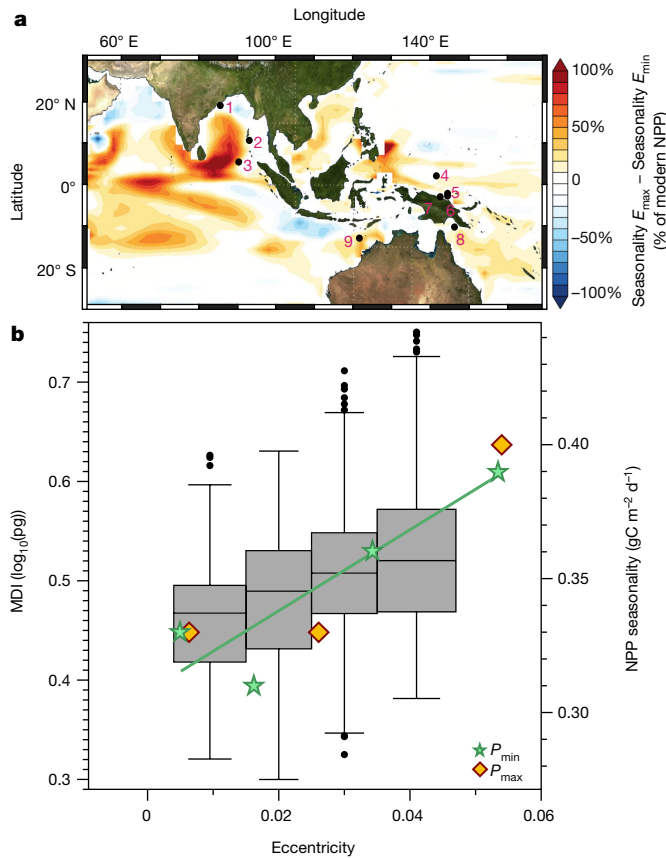


**Fig. 3 | Modelled NPP seasonal contrast under different eccentricity configurations and MDI.** **a**, Eccentricity-driven changes in the seasonality of NPP in the tropical Indo-Pacific. Colour scale shows the vertically integrated NPP seasonal contrast difference between numerical model outputs computed at maximum and minimum eccentricity, each run at perihelion in June ( $P_{\min}$ ) and December ( $P_{\max}$ ) and then averaged (Methods) (that is,  $\text{Seasonality } E_{\max} - \text{Seasonality } E_{\min}$ ). Values are expressed as a percentage of mean annual pre-industrial NPP simulated in a previous report<sup>5</sup>. Red colours imply higher seasonality at high eccentricity; blue colours imply higher seasonality at low eccentricity. Black circles show sediment core site locations used in this study: 1, IODP U1446; 2, IODP U1448; 3, IODP U1443; 4, MD97-2140; 5, MD05-2920; 6, IODP U1486; 7, IODP U1485; 8, MD05-2930; 9, IODP U1483 (Extended Data Table 1). Exact core locations are not relevant, as recorded evolutionary events may have originated anywhere in the tropics. **b**, Box-and-whiskers plots of all MDI values (centre line, median; box limits, first and third quartiles; whiskers, 1.5× inner quartile range; points, outliers), sorted by increasing low-pass-filtered eccentricity and grouped into four bins ( $e < 0.01$  (number of samples,  $n = 179$ );  $0.015 < e < 0.025$  ( $n = 328$ );  $0.025 < e < 0.035$  ( $n = 513$ ); and  $e > 0.035$  ( $n = 386$ )), compared to the seasonal NPP contrast (maximum minus minimum month) from seven numerical simulations (Methods). Model points represent a regional mean of the entire map area in **a**. As in Fig. 1b, orange diamonds are model runs with perihelion in December ( $P_{\max}$ ; 2,222 ka, 2,265 ka and 2380 ka), green stars are runs with perihelion in June ( $P_{\min}$ ; 2,230 ka, 2,346 ka, 2,369 ka, and 2,395 ka)—illustrating that eccentricity has a much larger effect on seasonality than precession at a given eccentricity.

Noelaerhabdaceae evolution and production throughout the Pleistocene. Although these changes clearly affect carbonate accumulation patterns (Fig. 1g), coccolithophore productivity alone cannot be responsible for the expression of long eccentricity cycles in climate records because they are only one constituent of the phytoplankton. Other phytoplankton groups, some with little or no fossil record, may also have been similarly influenced by variations in tropical seasonality on these timescales. In this case, the effect of changes in the ratio of exported organic carbon production to carbonate mineral production,

known as the rain ratio<sup>38</sup>, may have been strong enough to modulate the carbon cycle. The cyclic evolution of calcifying phytoplankton on eccentricity timescales in response to seasonality documented here provides evidence in support of the hypothesis that biosphere productivity must have responded to changes in solar insolation<sup>35,37</sup> to explain the strong e405 signature in carbon cycle records.

## Online content

Any methods, additional references, Nature Research reporting summaries, source data, extended data, supplementary information, acknowledgements, peer review information; details of author contributions and competing interests; and statements of data and code availability are available at <https://doi.org/10.1038/s41586-021-04195-7>.

1. Beaufort, L. et al. Sensitivity of coccolithophores to carbonate chemistry and ocean acidification. *Nature* **476**, 80–84 (2011).
2. Henderiks, J. & Böllmann, J. The Gephyrocapsa sea surface palaeothermometer put to the test: comparison with alkenone and foraminifera proxies off NW Africa. *Mar. Micropaleontol.* **50**, 161–184 (2004).
3. Bendef, E. M. et al. Repeated species radiations in the recent evolution of the key marine phytoplankton lineage Gephyrocapsa. *Nat. Commun.* **10**, 4234 (2019).
4. Ruddiman, W. F. & Raymo, M. E. Northern Hemisphere climate regimes during the past 3 Ma: possible tectonic connections. *Phil. Trans. R. Soc. B. Biol. Sci.* **318**, 411–430 (1988).
5. Sepulchre, P. et al. IPSL-CM5A2—an Earth System Model designed for multi-millennial climate simulations. *Geosci. Model Dev.* **13**, 3011–3053 (2020).
6. Aumont, O., Ethé, C., Tagliabue, A., Bopp, L. & Gehlen, M. PISCES-v2: an ocean biogeochemical model for carbon and ecosystem studies. *Geosci. Model Dev.* **8**, 2465–2513 (2015).
7. Broecker, W. & Clark, E. Ratio of coccolith  $\text{CaCO}_3$  to foraminifera  $\text{CaCO}_3$  in late Holocene deep sea sediments. *Paleoceanography* **24**, PA3205 (2009).
8. Sucheras-Marx, B. et al. The colonization of the oceans by calcifying pelagic algae. *Biogeosciences* **16**, 2501–2510 (2019).
9. Ridgwell, A. & Zeebe, R. E. The role of the global carbonate cycle in the regulation and evolution of the Earth system. *Earth Planet. Sci. Lett.* **234**, 299–315 (2005).
10. Young, J. et al. A guide to extant coccolithophore taxonomy. *Journal of Nannoplankton Research, Special Issue* **1**, 1–132 (2003).
11. Henderiks, J. Coccolithophore size rules—reconstructing ancient cell geometry and cellular calcite quota from fossil coccoliths. *Mar. Micropaleontol.* **67**, 143–154 (2008).
12. Filatov, D. A. Extreme Lewontin's paradox in ubiquitous marine phytoplankton species. *Mol. Biol. Evol.* **36**, 4–14 (2019).
13. Bown, P. R. Calcareous nannoplankton evolution: a tale of two oceans. *Micropaleontology* **51**, 299–308 (2005).
14. Si, W. & Rosenthal, Y. Reduced continental weathering and marine calcification linked to late Neogene decline in atmospheric  $\text{CO}_2$ . *Nat. Geosci.* **12**, 833–838 (2019).
15. Bolton, C. T. et al. Decrease in coccolithophore calcification and  $\text{CO}_2$  since the middle Miocene. *Nat. Commun.* **7**, 10284 (2016).
16. Gibbs, S. J., Shackleton, N. & Young, J. Orbitally forced climate signals in mid-Pliocene nanofossil assemblages. *Mar. Micropaleontol.* **51**, 39–56 (2004).
17. Beaufort, L. et al. Insolation cycles as a major control of equatorial Indian Ocean primary production. *Science* **278**, 1451–1454 (1997).
18. Chepstow-Lusty, A., Backman, J. & Shackleton, N. J. Comparison of upper Pliocene Discoaster abundance variations from North Atlantic Sites 552, 607, 658, 659 and 662: further evidence for marine plankton responding to orbital forcing. *Proc. ODP Sci. Results* **108**, 121–141 (1989).
19. Thierstein, H. R., Geitzenauer, K. R., Molino, B. & Shackleton, N. J. Global synchrony of late Quaternary coccolith datum levels: validation by oxygen isotopes. *Geology* **5**, 400–404 (1977).
20. Böllmann, J., Baumann, K. H. & Thierstein, H. R. Global dominance of Gephyrocapsa coccoliths in the Late Pleistocene: selective dissolution, evolution, or global environmental change? *Paleoceanography* **13**, 517–529 (1998).
21. Raffi, I. et al. A review of calcareous nanofossil astrobiochronology encompassing the past 25 million years. *Quat. Sci. Rev.* **25**, 3113–3137 (2006).
22. Lisicki, L. E. & Raymo, M. E. A Pliocene–Pleistocene stack of 57 globally distributed benthic  $\delta^{18}\text{O}$  records. *Paleoceanography* **20**, PA1003 (2005).
23. Laskar, J. et al. A long-term numerical solution for the insolation quantities of the Earth. *Astron. Astrophys.* **428**, 261–285 (2004).
24. Okada, H. & McIntyre, A. Seasonal distribution of modern Coccolithophores in the western North Atlantic ocean. *Mar. Biol.* **54**, 319–328 (1979).
25. Longhurst, A. *Ecological Geography of the Sea Vol. 1* (Academic Press, 1998).
26. Sexton, P. F. & Barker, S. Onset of ‘Pacific-style’ deep-sea sedimentary carbonate cycles at the mid-Pleistocene transition. *Earth Planet. Sci. Lett.* **321–322**, 81–94 (2012).
27. Rickaby, R. E. M. et al. Coccolith chemistry reveals secular variations in the global ocean carbon cycle? *Earth Planet. Sci. Lett.* **253**, 83–95 (2007).
28. Wang, P., Tian, J. & Lourens, L. J. Obscuring of long eccentricity cyclicity in Pleistocene oceanic carbon isotope records. *Earth Planet. Sci. Lett.* **290**, 319–330 (2010).
29. Sucheras-Marx, B. & Henderiks, J. Downsizing the pelagic carbonate factory: impacts of calcareous nanoplankton evolution on carbonate burial over the past 17 million years. *Glob. Planet. Change* **123**, 97–109 (2014).
30. Holligan, P. M. et al. A biogeochemical study of the coccolithophore, *Emiliania huxleyi*, in the North Atlantic. *Global Biogeochem. Cycles* **7**, 879–900 (1993).

31. Laepple, T. & Lohmann, G. Seasonal cycle as template for climate variability on astronomical timescales. *Paleoceanography* **24**, PA4201 (2009).
32. Righetti, D., Vogt, M., Gruber, N., Psomas, A. & Zimmermann, N. E. Global pattern of phytoplankton diversity driven by temperature and environmental variability. *Sci. Adv.* **5**, eaau6253 (2019).
33. Ruddiman, W. F., Raymo, M. & McIntyre, A. Matuyama 41,000-year cycles : North Atlantic Ocean and Northern hemisphere ice sheets. *Earth Plan. Sci. Lett.* **80**, 117–129 (1986).
34. Zeebe, R. E., Westerhold, T., Littler, K. & Zachos, J. C. Orbital forcing of the Paleocene and Eocene carbon cycle. *Paleoceanography* **32**, 440–465 (2017).
35. Pälike, H. et al. The heartbeat of the Oligocene climate system. *Science* **314**, 1894–1898 (2006).
36. Herbert, T. D. A long marine history of carbon cycle modulation by orbital-climatic changes. *Proc. Natl Acad. Sci. USA* **94**, 8362–8369 (1997).
37. Ma, W., Tian, J., Li, Q. & Wang, P. Simulation of long eccentricity (400-kyr) cycle in ocean carbon reservoir during Miocene Climate Optimum: weathering and nutrient response to orbital change. *Geophys. Res. Lett.* **38**, L10701 (2011).
38. Archer, D. & Maier-Reimer, E. Effect of deep-sea sedimentary calcite preservation on atmospheric CO<sub>2</sub> concentration. *Nature* **367**, 260–263 (1994).

**Publisher's note** Springer Nature remains neutral with regard to jurisdictional claims in published maps and institutional affiliations.

© The Author(s), under exclusive licence to Springer Nature Limited 2021

## Methods

### Acquisition of coccolith data

Over 8,000 samples were extracted from sediment cores for coccolithophore analysis at depth intervals to achieve a high stratigraphic resolution (0.5 to 2.3 kyr; Extended Data Table 1). Samples were prepared using the settling method<sup>39,40</sup>: sediments were disaggregated in water and suspensions were settled onto a 12 × 12-mm cover slip and mounted with Norland Optical Adhesive 74, with 8 cover slips per microscope slide. Some samples were prepared as independent duplicates. Two slides (16 samples) were placed onto the stage of an automated polarizing microscope (Leica DM6000). After auto-focusing, 165 contiguous fields of view (with an area of 125 × 125 µm each) were imaged in each sample using a black and white SPOTFLEX camera (Diagnostic Instrument). SYRACO, a software program based on an artificial neural network<sup>41</sup>, identified all specimens belonging to 33 groups of coccolithophore taxa in the images<sup>42</sup>. The gephyrocapsid specimens—the dominant group studied here—were classified into six distinct classes that were merged into one group. On average, 888 Noelaerhabdaceae coccoliths were identified in each sample. Among other morphometric parameters, the size and mass of the coccoliths were measured. Coccolith mass is measured using birefringence, following published state-of-the-art methods<sup>40,43</sup>. The use of artificial intelligence in this type of work is essential because it is the only way to measure such a large number of specimens (more than 7 million) in a reasonable time, and thus obtain the high-resolution multi-site records required for this study.

The pattern recognition was performed with a structured multi-layer neural network called SYRACO, written in C++ by D. Dollfus<sup>44</sup>. The input image of 64 × 64 pixels is connected to the output (class name) by three convolutional layers of 1,764, 360 and 80 neurons with no shared weights, which induces a long computing time. The advantages of this structure are discussed in a previous study<sup>45</sup>. To mimic the dynamic process of human recognition, in parallel to the second and third convolutional layers, there are 3 small neural networks of 20 neurons each, called motor layers, that perform simple image transformations from 5 possibilities: rotation, translation, symmetry, contrast and dilation. These parallel neural networks enhance the efficiency of the pattern recognition by 50% (ref. <sup>41</sup>) with an accuracy above 95% (based on more than 5,000 test images). In his PhD thesis, N.B. increased the number of calcareous nannofossil species recognized by SYRACO to include most Cenozoic species and grouped them into 49 morphological classes<sup>42</sup>. The number of false positives (non-coccolith particles of calcareous debris such as broken foraminifera, micrite and broken coccoliths) has been reduced in SYRACO by adding a second pattern recognition level after the SYRACO artificial neural network (ANN), based on a random forest algorithm<sup>46</sup>. This cross-checking is more robust because it results in only 5% of false positives, compared to around 50% before<sup>42</sup>. In this work, we combine the 49 morphological classes into only 5 groups and work essentially with one of these, the Noelaerhabdaceae. From the confusion matrix produced by the analysis of 6,888 images (ref. <sup>42</sup>, table 1, p.109), the percentage of successful identifications for those 5 taxonomic groups is 96% for Noelaerhabdaceae; 91% for Coccolithales; 90% for Syracospherales and Zygodiscates (grouped together); and 88% for other coccolith taxa. *Florisphaera profunda* coccoliths are recognized at a rate of 98% (ref. <sup>42</sup>). Most of the losses can be explained by the quality of the captured image, owing to some particle in a large image being out of focus or luminosity and contrast problems, or aggregation of particles. We progressively solved some of these problems by developing new optical methods<sup>40,43</sup> and by changing the pre-processing (for example, refining image segmentation); this increased the number of recognized coccoliths without changing the proportion of the different species. Because we were satisfied with its performance, we did not test other architectures

of SYRACO such as increasing the number and the size of the convolutional layers. The goal of SYRACO was to provide a robust and rapid coccolith extractor compatible with commercial computer performance during development in the late 1990s and early 2000s. In this work, SYRACO was processed on a Dell Precision T7910 with 2 Xeon processors (2.3 GHz) of 20 cores each and 64 GB of memory, with Windows as the operating system.

### Site-specific chronologies

**IMAGES core MD97-2140.** The age model for site MD97-2140<sup>47</sup>, on the Eauripik Rise in the Western Pacific Warm Pool, is based on tuning of a high-resolution planktonic foraminiferal *Globigerinoides ruber* δ<sup>18</sup>O record to the astronomically calibrated ODP site 677 δ<sup>18</sup>O *G. ruber* record<sup>48</sup>, located in the eastern equatorial Pacific. This age model yields a chronology consistent with major micropaleontological (disappearance of *G. ruber* pink variety) and palaeomagnetic (Brunhes–Matuyama boundary) events<sup>49</sup>.

**IMAGES core MD05-2920.** The age model for site MD05-2920<sup>50,51</sup>, on the southern bank of Manus Island, is based on 10 accelerator mass spectrometer (AMS) <sup>14</sup>C dates obtained from the surface-dwelling planktonic foraminifera *G. ruber* (white), and a correlation between the benthic foraminiferal δ<sup>18</sup>O record and the reference LR04 benthic foraminiferal δ<sup>18</sup>O stack<sup>22</sup>.

**IMAGES core MD05-2930.** The age model for site MD05-2930<sup>50,52</sup>, in the Coral Sea, is based on 10 AMS <sup>14</sup>C measurements of *G. ruber sensu stricto* (ss), and on correlation of the MD05-2930 δ<sup>18</sup>O *G. ruber ss* record with the LR04 benthic foraminiferal δ<sup>18</sup>O stack<sup>22</sup>.

**IODP site U1443.** The age model for site U1443<sup>53</sup>, on the Ninetyeast Ridge in the southernmost Bay of Bengal, is based on correlation of physical properties data on the primary shipboard splice to the LR04 benthic foraminiferal δ<sup>18</sup>O stack<sup>22</sup>. Physical properties were measured onboard the RV *Joides Resolution* on archive halves from all holes at site U1443, and correlation and splicing were based on magnetic susceptibility, natural gamma ray and reflectance spectroscopy b\* data<sup>54</sup>.

**IODP site U1448.** The age model for site U1448<sup>53</sup>, in the Andaman Sea, is based on correlation of the site U1448 Ti/Ca record, derived by X-ray fluorescence (XRF) core scanning, to the XRF Ti/Ca record of Indian National Gas Hydrate Program (NGHP) site 17—a very close site with age control based on a benthic foraminiferal oxygen isotope record tuned to the LR04 benthic foraminiferal δ<sup>18</sup>O stack<sup>22,55,56</sup>.

**IODP site U1446.** The age model for Mahanadi Basin Site U1446<sup>53</sup> is based on correlation of a high-resolution benthic foraminiferal oxygen isotope stratigraphy to the LR04 benthic foraminiferal δ<sup>18</sup>O stack<sup>22,57</sup>.

**IODP site U1483.** The age model for Scott Plateau Site U1483<sup>58</sup> is based on the shipboard integrated magneto-biostratigraphy, and on correlation of the U1483 L\* record, which presents strong G–IG variability, to the LR04 benthic foraminiferal δ<sup>18</sup>O stack<sup>22</sup>.

**IODP site U1485.** The age model of the northern Papua margin site U1485<sup>58</sup> is based on correlation between the benthic foraminiferal δ<sup>18</sup>O record of this site and the LR04 benthic foraminiferal δ<sup>18</sup>O stack<sup>22</sup>.

**IODP site U1486.** The age model of the upper 100 m (the last 1.6 Ma) of site U1486<sup>58</sup>, from the southern bank of Manus Island, is based on a correlation between the benthic foraminiferal δ<sup>18</sup>O record and the LR04 benthic foraminiferal δ<sup>18</sup>O stack<sup>22</sup>. Below 100 m, the age model is based on the shipboard integrated magneto-biostratigraphy and correlation of the U1486 L\* record (that shows strong G–IG variability) with the LR04 benthic foraminiferal δ<sup>18</sup>O stack<sup>22</sup>.

## Construction of composite frequency contour plot of coccolith size

Measurements were grouped into morphological bins of  $0.1\text{ }\mu\text{m}$  for coccolith length in every sample. Samples were binned into 30-kyr time windows in each core, chosen such that it is larger than the length of a precession cycle (23–19 kyr). This will prevent any bias in the size and mass distribution resulting from changes in the relative abundance of large versus small gephyrocapsid species on precessional timescales<sup>59</sup>. Another advantage of using a 30-kyr time window is that the high number of measurements included in each bin (on average 16,650 measurements) makes it extremely precise but easier to discern trends. To standardize each time window at each site, the numbers contained in each bin are divided by the total number of coccoliths in that time window and multiplied by 100. To stack the records and produce the frequency-density plot of size (Fig. 1a), samples in each core were grouped into 30-kyr bins, standardized (%) and merged into a single stack. Frequency contour plots for size and mass (the latter not shown) show near-identical trends and variability. The distribution of coccolith mass values is skewed toward heavy values. We therefore used the logarithm of the mass to obtain a symmetrical mass distribution before binning (0.05 log(pg) bins) and stacking as for length.

## Note on taxonomy of the Pleistocene Noelaerhabdaceae

The genus concept in the Pleistocene Noelaerhabdaceae is rather straightforward<sup>10,60</sup>: *Emiliania* presents ‘T-shaped’ elements in its distal shield, *Gephyrocapsa* presents a bridge in its central area, *Pseudoemiliania* presents slits in its distal shield and *Reticulofenestra* has none of these features. Two of these features may be present on *Gephyrocapsa* (for example, *Gephyrocapsa protohuxleyi*). The species concept is much more complex<sup>10,60,61</sup>. It essentially depends on coccolith size, ratio of central area opening to coccolith size, and bridge angle (for *Gephyrocapsa*). All of these features are continuous rather than discrete parameters and therefore often present a continuum between species. In Fig. 1a, b, the size density plot and the average size plot illustrate how size is a variable feature. One of the main taxonomic parameters of this group (that is, size) is constantly evolving, complicating the common use of a size-based typological species concept. A previous study<sup>3</sup> indicates that all extant species evolved from *G. caribbeanica* around 550,000 years ago, implying a rapid (less than 0.55 Myr) species turnover. The Noelaerhabdaceae family is therefore rapidly evolving genetically and morphologically. In this paper we do not intend to dispute taxonomy or species concepts. Given that it is difficult to follow genetic and typological species through time in this family, we prefer to discuss morphological evolution in a taxon-free manner. In the described taxonomies of this family<sup>60</sup>, there remains however a clear cut-off at around  $3\text{ }\mu\text{m}$  between coccoliths of smaller and larger Noelaerhabdaceae species, which is why we choose this boundary to develop the MDI concept.

## MDI

To quantitatively capture the history of biological evolution within a group of species with a biometric tool, it is necessary to build a metric that it is as independent as possible from the population dynamics of the different species relative to the others. This is because the biometry of a multi-species population is greatly influenced by its population dynamics: the relative success of one species in one particular biotope will affect the average biometry of the entire population. The average biometry is therefore greatly influenced by species adaptation to biotopes and will not be necessarily diagnostic of biological evolution. A way to limit the influence of the relative abundance of species in a sample is to measure the difference between the biometric means of the considered species. A simple index can be designed to parametrize a biometric boundary between two populations: the arithmetic distance between the two population means. A schematic example of an evolutionary sequence as recorded by MDI is described in Fig. 2a.

Therefore, the MDI is not designed: (1) to trace the spatial variation of ecological parameters such as seasonality. This is because a new morphological trait will spread rapidly (on geological timescales) in the ocean if it is successful. The MDI will be distributed evenly wherever the species are present; or (2) to describe a physiological adaptation to a fluctuating environment. MDI is designed (1) to trace the morphological evolution of a small group of species; (2) to trace temporal variations of ecological parameters at the large geographical scale that can lead to the evolution of new morphological traits.

## MDI designed for Plio-Pleistocene Noelaerhabdaceae

In each sample, individual coccoliths were divided into two size classes: coccoliths longer and shorter than  $3\text{ }\mu\text{m}$ . The average log(mass) is calculated in both classes. MDI is the difference between the two averages (Fig. 2b). The size of  $3\text{ }\mu\text{m}$  corresponds to the best cut-off value between the two modes ( $2.8$  and  $3.9\text{ }\mu\text{m}$ ) of the size distribution. Other size cut-offs ( $2.9$ ,  $3.25$  and  $3.5\text{ }\mu\text{m}$ ) as well as a mass cut-off ( $3.16\text{ pg}$ ) were tested, without large differences in the resulting MDI values and temporal trends (Fig. 2b). The records are resampled (by linear integration) at 2-kyr intervals for further analysis (time series, statistics, and stacking). A stacked record composed of all records is calculated for each time window. This stacked MDI reflects the variability seen in all individual records (Extended Data Fig. 1). Because not all records cover the entire 2.8-Myr interval (3 records are over 2.3 Myr long, 3 are between 0.7 and 1.8 Myr long and 3 are 0.4–0.6 Myr long), the stack is composed of more records in the younger part than in the older part. Because of the phase lag between MDI and eccentricity we use band-passed eccentricity (red line in Fig. 1b) to sort and bin MDI values used for Fig. 3b. Finally, because the relative abundances of small versus larger Noelaerhabdaceae are not considered during the calculation of the MDI, any preferential dissolution of smaller more fragile coccoliths would not affect the MDI, as it represents the difference between the mean masses of the two size groups. A negligible effect of carbonate dissolution on MDI is supported by the fact that species-specific mean coccolith mass is conserved in dissolution experiments<sup>62</sup>, and by the similarity between MDI records regardless of core depth in the range of around 1,100–3,000 m (all well above the Pleistocene Pacific carbonate saturation horizon) (Extended Data Fig. 1).

## Mass accumulation rates

Mass accumulation rates of Noelaerhabdaceae coccoliths (NoMARs) were estimated in seven cores (all cores excluding MD05-2530 and U1446), for which a quantitative sample preparation technique was applied<sup>40</sup>. The samples were prepared by settling onto coverslips that were weighed before and after settling, the weight difference providing the amount of sediment deposited. The number and the mass of the Noelaerhabdaceae is estimated by SYRACO. From these quantities it is possible to estimate the weight of Noelaerhabdaceae per gram of sediment. NoMAR is obtained by multiplying weight per gram by the sedimentation rate and the dry bulk density of sediment. The dry bulk density was estimated from continuous measurements of wet bulk density from gamma ray attenuation (GRA) and transformed by the linear relationship for each site between discrete shipboard measurements of wet bulk density and dry bulk density<sup>63</sup>. NoMARs for the 7 cores were stacked together after resampling each record at 2-kyr intervals (Fig 1g), using the same method as for MDI. Other stacking methods, such as assembling Loess-detrended records, were tried and produced consistent results. Differences exist between individual NoMAR records owing to regional difference in coccolithophore productivity, export dynamics and core depth (although only 2 cores, MD97-2140 and U1443, were retrieved from sediments deeper than 2,000 m). However, three common patterns emerge in all individual records: an increasing trend in NoMAR towards the present, a stepwise increase at around 1.1 Ma and the clear presence of eccentricity cycles. Noelaerhabdaceae coccolith flux (Extended Data Fig. 3b) is calculated as the number of coccoliths

per gram of sediment multiplied by the sedimentation rate, and is the main driver of the step increase in NoMAR at around 1.1 Ma.

### Time-series analysis

Time-series analyses were performed using the software packages Analyseries<sup>64</sup> and Acycle<sup>65</sup> on detrended records. Cross-spectral analyses were performed in Analyseries using Blackman–Turkey transforms<sup>66</sup>. For evolutive cross-spectral analyses (Fig. 1d, f) a window of 500 kyr (250 data points) and a step of 100 kyr was used. Coherence values above 0.56 are above the 80% confidence level. Spectral analyses were performed with the multi-taper method (MTM)<sup>67</sup> with both evolutive and entire series (Extended Data Fig. 2). Spectral properties are similar in all individual MDI records, and show that the absence of precession (19–23 kyr) and obliquity (around 41 kyr) is not a result of chronological bias in constructing the stack that would have smoothed the record. Each record has a resolution of around 2 kyr with a precise independent age model. The absence of precession and obliquity is therefore a common and robust feature of all of the MDI series as well as the stacked record.

### Low-pass filters

We designed second-order low-pass filters to reproduce the effect of the time needed for a new evolved species to fully succeed (200 kyr for *E. huxleyi*). We transformed the following classical low-pass filter complex transfer function  $H$ :

$$H(j\omega) = \frac{A}{1 + \frac{j}{Q} \frac{\omega}{\omega_0} - \frac{\omega^2}{\omega_0^2}}$$

(where  $A$  is the amplitude,  $Q$  is the quality factor,  $\omega$  is the angular frequency  $2\pi f$  (the frequency)) in its associated differential equation:

$$\frac{d^2y}{dt^2} + \frac{\omega_0}{Q} \frac{dy}{dt} + \omega_0^2 y = \omega_0^2 x,$$

where  $y$  is the output series and  $x$  the input series.

We solved it numerically as follows:

$$y_t = \frac{1}{1 + \frac{\omega_0}{Q}} \left( (2 + \omega_0) y_{t-1} - y_{t-2} \right) A \omega_0^2 x_t$$

Two configurations have been chosen: one produces a delay of 200 kyr for the new species' success, the second produces a delay of 130 kyr (Extended Data Fig. 7a). To obtain those delays, we used the following values:

First case (delay of 200 kyr),  $\omega_0 = 0.021$ ,  $Q = 1$ ,  $A = 1$ ;  
Second case (delay of 130 kyr),  $\omega_0 = 0.035$ ,  $Q = 1.02$ ,  $A = 0.65$ .

The delay of 200 kyr corresponds to the time between the first appearance datum (FAD) and the beginning of the acme (BA) of *E. huxleyi*<sup>21</sup>. The FAD of this species is well documented because its characteristic T-shaped elements are a morphological feature that appeared suddenly, without gradation. The other *Gephyrocapsa* species have been described using criteria that are subject to gradation between species: coccolith length, size of the central opening, and orientation of the bridge<sup>68</sup>. For example, the FAD of a typical *G. ericsonii*, (a small gephyrocapsid) that appeared at about the same time as *E. huxleyi*<sup>3</sup> is not reported precisely because it evolved progressively from *G. caribeanica* (a mid-size species). It is interesting to note that the FAD and the BA of *E. huxleyi* occurred similarly in times of eccentricity decrease, but two cycles apart. The intermediate cycle may have been too high to allow *E. huxleyi* to begin its dominance. This may not have been the case for other species under different orbital configurations. This is why we did a filter with a different configuration, which produces a delay

of about one eccentricity cycle between a FAD and a BA. To express the response of those filters, we built their Bode magnitude plots, expressing the frequency response, and their Bode phase plots, expressing the phase shift (Extended Data Fig. 7b, c).

### Model description

To simulate changes in NPP related to changes in eccentricity we used the Earth System Model IPSL-CM5A2<sup>5</sup> that simulates the interactions between ocean, atmosphere, land and ice. The following section provides a brief description of model components and experimental set-up. We then describe the model behaviour at low eccentricity and discuss how the large-scale ocean–atmosphere circulation at high eccentricity in our simulations compares to previous modelling studies.

The IPSL-CM5A2 coupled model is a combination of the LMDZ5A atmospheric model<sup>69</sup>, the ORCHIDEE<sup>70</sup> land surface model and the NEMO v.3.6 oceanic model<sup>71</sup>. The NEMO model includes an ocean dynamic component (OPA<sup>72</sup>) and a sea-ice thermodynamics model (LIM2<sup>73</sup>), as well as a biogeochemistry model (PISCES-v2<sup>6</sup>), and has an horizontal resolution of 2° by 2° (refined to 0.5° in the tropics) and 31 vertical levels, the thickness of which increases from 10 m at the surface to 500 m at the bottom. The atmospheric grid has a horizontal resolution of 1.875° in latitude by 3.75° in longitude with 39 vertical levels. The ocean–atmosphere coupling is ensured by the OASIS coupler<sup>74</sup> that interpolates and exchanges variables between the two components. Detailed descriptions of IPSL-CM5A2 and performances in simulating pre-industrial climate can be found in previous reports<sup>5,75</sup>. PISCES-v2 simulates the main oceanic biogeochemical cycles (C, P, Si, N and Fe) and has a simple representation of the lower trophic levels of the marine ecosystem<sup>6</sup>, with two phytoplankton (nannophytoplankton and diatoms) and two zooplankton (micro- and mesozooplankton) size classes and five limiting nutrients (Fe, NO<sub>3</sub><sup>-</sup>, NH<sub>4</sub><sup>+</sup>, Si and PO<sub>4</sub><sup>3-</sup>). Phytoplankton growth is controlled by nutrients, light availability and water temperature. In the version of the model we used, river supply to the ocean of all elements apart from dissolved inorganic carbon and alkalinity is taken from the GLOBAL-NEWS2 datasets<sup>76</sup> and does not vary from one simulation to another. Model parameterizations are detailed in a previous report<sup>6</sup>.

Simulations were performed for seven early Pleistocene time slices and differ only by their respective orbital parameters (Extended Data Table 3, Fig. 1b). The time slices were chosen to target the signal produced by the 405-kyr eccentricity cycle. Land–sea mask, ice-sheet configuration as well as CO<sub>2</sub> and other greenhouse gases concentrations are set at pre-industrial values. Each simulation was started from the same equilibrated pre-industrial simulation<sup>5</sup> and was run for 500 years. NPP is integrated over the whole water column and averaged over the last 100 model years.

At low eccentricity ( $E_{\min} P_{\max}$  and  $E_{\min} P_{\min}$ ) the eastern Indian ocean surface dynamics are forced by the summer westerlies that blow northward over the Bay of Bengal (Extended Data Fig. 4f), associated with high precipitation over India and the Himalayan foreland region, whereas strong easterlies are recorded south of the equator. Winds force strong westward surface currents along the equator and south of Sumatra that generate upwelling (Extended Data Fig. 7b). The latter advects nutrients to the surface (Extended Data Fig. 7a) and triggers high productivity during summer. This peak productivity contributes to the strong seasonal cycle in this region. The winds reverse during boreal winter, triggering a second productivity bloom of lesser intensity (not shown). The productivity minimum is recorded during late spring when low-level winds along the equator are weak westerlies that favour downwelling and prevent strong convective mixing, which results in lower nutrient content within the surface layer of the ocean. The seasonal cycle of productivity in this region is very similar to the cycle simulated for the present-day equatorial Indian Ocean<sup>5</sup>.

During high eccentricity periods at precession minima (maxima), increasing (decreasing) boreal summer insolation (Extended Data

# Article

Fig. 5b,c) is responsible for increasing (decreasing) sea-level pressure over continental Asia (Extended Data Fig. 5d–h). Induced modifications of sea-level pressure gradients over the tropical Indian and Pacific Oceans in turn translate into changes in the low-level wind circulation over the IPWP (Extended Data Fig. 4f–h). Anomalous easterlies at precession minima (westerlies at precession maxima) in the equatorial region generate anomalous upwelling along the equator (southwest of India) that are responsible for the increasing nutrient content at the surface triggering large enhancement of productivity (Extended Data Fig. 6a–c). NPP is, in addition, amplified by modifications of the hydrological cycle that create more favourable conditions related to changes in salinity, water temperature and/or amount of solar radiation at the surface. At maximum precession and eccentricity, for example, higher sub-surface salinity (+0.5 to 1.6 psu) and lower temperatures (−1.2 to −2 °C) in the western Bay of Bengal (Extended Data Fig. 7c) reduce stratification of the upper-water column, which favours vertical mixing and contributes to enhanced productivity. The simulated patterns of atmosphere–ocean circulation and surface ocean physical state (Extended Data Figs. 4f–h, 6b, c) are in line with previous modelling studies under similar orbital configurations<sup>77–79</sup>. In addition, our simulations also illustrate how these changes affect the seasonal productivity cycle. The increasing amplitude of the seasonal cycle in the surface ocean at high eccentricity is probably not limited to the IPWP area. For example, another study<sup>80</sup> also simulates enhancement of the surface ocean temperature cycle at high eccentricity in the Eastern Equatorial Pacific, with higher amplitude than in the Western Equatorial Pacific.

## Reporting summary

Further information on research design is available in the Nature Research Reporting Summary linked to this paper.

## Data availability

All coccolith morphological data, as well as all model outputs described in the paper (including NPP and main oceanic and atmospheric variables) are archived at the SEANOE open access data repository: <https://doi.org/10.17882/84031>. LMDZ, XIOS, NEMO and ORCHIDEE are released under the terms of the CeCILL license. OASIS-MCT is released under the terms of the Lesser GNU General Public License (LGPL). IPSL-CM5A2 source code is publicly available through svn, with the following commands line : svn co <http://forge.ipsl.jussieu.fr/igcmg/> svn/modipsl/branches/publications/IPSLCM5A2.1\_1192019 modipsl ; cd modipsl/util ; ./model IPSLCM5A2.1. The mod.def file provides information regarding the different revisions used, namely: NEMOGCM branch nemo\_v3\_6\_STABLE revision 6665; XIOS2 branchs/xios-2.5 revision 1763; IOIPSL/src svn tags/v2\_2\_2; LMDZ5 branches/IPSLCM5A2.1 rev 3591; branches/publications/ORCHIDEE\_IPSLCM5A2.1.r5307 rev 6336; and OASIS3-MCT 2.0\_branch (rev 4775 IPSL server). The login/password combination requested at first use to download the ORCHIDEE component is anonymous/anonymous. We recommend that you refer to the project website: [http://forge.ipsl.jussieu.fr/igcmg\\_doc/wiki/Doc/Config/IPSLCM5A2](http://forge.ipsl.jussieu.fr/igcmg_doc/wiki/Doc/Config/IPSLCM5A2) for a proper installation and compilation of the environment.

39. Beaufort, L. Adaptation of the random settling method for quantitative studies of calcareous nannofossils. *Micropaleontology* **37**, 415–418 (1992).
40. Beaufort, L., Barbarin, N. & Gally, Y. Optical measurements to determine the thickness of calcite crystals and the mass of thin carbonate particles such as coccoliths. *Nat. Protoc.* **9**, 633–642 (2014).
41. Beaufort, L. & Dollfus, D. Automatic recognition of coccolith by dynamical neural network. *Mar. Micropaleont.* **51**, 57–73 (2004).
42. Barbarin, N. *La Reconnaissance Automatisée des Nannofossiles Calcaires du Cénozoïque*. PhD thesis, Aix-Marseille Univ. (2014).
43. Beaufort, L. Weight estimates of coccoliths using the optical properties (birefringence) of calcite. *Micropaleontology* **51**, 289–298 (2005).
44. Dollfus, D. *Reconnaissance des Formes Naturelles par des Réseaux de Neurones Artificiels: Application au Nannoplankton Calcaire*. PhD thesis, Aix-Marseille Univ. (1997).
45. Dollfus, D. & Beaufort, L. Fat neural network for recognition of position-normalised objects. *Neural Netw.* **12**, 553–560 (1999).
46. Breiman, L. Random forests. *Mach. Learn.* **45**, 5–32 (2001).
47. de Garidel-Thoron, T., Rosenthal, Y., Bassinot, F. C. & Beaufort, L. Stable sea surface temperatures in the western Pacific warm pool over the past 1.75 million years. *Nature* **433**, 294–298 (2005).
48. Shackleton, N. J. & Al, E. An alternative astronomical calibration of the lower Pleistocene timescale based on ODP Site 677. *Trans. R. Soc. Edinb. Earth Sci.* **81**, 251–261 (1990).
49. Carcaillet, J. T., Thouveny, N. & Bourlès, D. L. Geomagnetic moment instability between 0.6 and 1.3 Ma from cosmogenic evidence. *Geophys. Res. Lett.* **30**, 1792 (2003).
50. Beaufort, L. & Party, S. S. *MD148/PECTEN* (Institut Polaire Français, 2005).
51. Tachikawa, K. et al. The precession phase of hydrological variability in the Western Pacific Warm Pool during the past 400 ka. *Quat. Sci. Rev.* **30**, 3716–3727 (2011).
52. Regoli, F. et al. Progressive shoaling of the equatorial Pacific thermocline over the last eight glacial periods. *Paleoceanography* **30**, 439–455 (2015).
53. Clemens, S. C. et al. *Indian Monsoon Rainfall*. International Ocean Discovery Program Preliminary Report 353 (IODP Publications, 2015).
54. Clemens, S. C. et al. Site U1443. In *Proc. International Ocean Discovery Program Vol. 353*, <https://doi.org/10.14379/iodp.proc.353.103.2016> (2016).
55. Gebregiorgis, D. et al. Southern Hemisphere forcing of South Asian monsoon precipitation over the past ~1 million years. *Nat. Commun.* **9**, 4702 (2018).
56. Gebregiorgis, D. et al. What can we learn from X-ray fluorescence core scanning data? A paleomonsoon case study. *Geochem. Geophys. Geosyst.* **21**, e2019GC008414 (2020).
57. McGrath, S. M., Clemens, S. C., Huang, Y. & Yamamoto, M. Greenhouse gas and ice volume drive Pleistocene Indian summer monsoon precipitation isotope variability. *Geophys. Res. Lett.* **48**, e2020GL092249 (2021).
58. Rosenthal, Y. et al. Site U1485. In *Proc. International Ocean Discovery Program Vol. 363*, <https://doi.org/10.14379/iodp.proc.363.106.2018> (2018).
59. Beaufort, L., Bassinot, F. C. & Vincent, E. In *Reconstructing Ocean History: a Window into the Future* (eds Abrantes, F. & Mix, A. C.) 245–272 (Kluwer Academic/Plenum Publisher, 1999).
60. Young, J. R., P.R., Bown & J.A., Lees *Nannotax3* <http://www.mikrotax.org/Nannotax3> (2021).
61. Perch-Nielsen, K. in *Plankton Stratigraphy* Vol. 1 (eds Bolli, H. M., Saunders, J. B. & Perch-Nielsen, K.) (CUP Archive, 1989).
62. Beaufort, L., Probert, I. & Buchet, N. Effects of acidification and primary production on coccolith weight: Implications for carbonate transfer from the surface to the deep ocean. *Geochem. Geophys. Geosystems* **8**, Q08011 (2007).
63. Lyle, M. Neogene carbonate burial in the Pacific Ocean. *Paleoceanography* **18**, 1059 (2003).
64. Paillard, D., Labeyrie, L. & Yiou, P. Macintosh program performs time-series analysis. *Eos* **77**, 379 (1996).
65. Li, M., Hinno, L. & Kump, L. Acycle: time-series analysis software for paleoclimate research and education. *Comput. Geosci.* **127**, 12–22 (2019).
66. Blackman, R. B. & Tukey, J. W. The measurement of power spectra from the point of view of communications engineering—Part I. *Bell Syst. Tech. J.* **37**, 185–282 (1958).
67. Thomson, D. J. Spectrum estimation and harmonic analysis. In *Proc. IEEE* Vol. 70, 1055–1096 (1982).
68. Böllmann, J. Morphology and biogeography of the Gephyrocapsa coccoliths in Holocene sediments. *Mar. Micropaleont.* **29**, 319–350 (1997).
69. Hourdin, F. et al. Impact of the LMDZ atmospheric grid configuration on the climate and sensitivity of the IPSL-CM5A coupled model. *Clim. Dyn.* **40**, 2167–2192 (2013).
70. Krinner, G., Ciais, P., Viovy, N. & Friedlingstein, P. A simple parameterization of nitrogen limitation on primary productivity for global vegetation models. *Biogeosciences Discuss.* **2**, 1243–1282 (2005).
71. Madec, G. & Nemo, T. *NEMO Ocean Engine*. Note du Pôle de modélisation de l’Institut Pierre-Simon Laplace no. 27 (IPSL, 2015).
72. Madec, G. *NEMO Reference Manual, Ocean Dynamics Component: NEMO-OPA*. Preliminary Version. Note du Pôle de modélisation de l’Institut Pierre-Simon Laplace (IPSL, 2008).
73. Fichefet, T. & Maqueda, M. M. Sensitivity of a global sea ice model to the treatment of ice thermodynamics and dynamics. *J. Geophys. Res. Oceans* **102**, 12609–12646 (1997).
74. Valcke, S. et al. Coupling technologies for earth system modelling. *Geosci. Model Dev.* **5**, 1589–1596 (2012).
75. Dufresne, J.-L. et al. Climate change projections using the IPSL-CM5 Earth System Model: from CMIP3 to CMIP5. *Clim. Dyn.* **40**, 2123–2165 (2013).
76. Mayorga, E. et al. Global nutrient export from WaterSheds 2 (NEWS 2): model development and implementation. *Environ. Modelling Softw.* **25**, 837–853 (2010).
77. Bosmans, J. et al. Response of the Asian summer monsoons to idealized precession and obliquity forcing in a set of GCMs. *Quat. Sci. Rev.* **188**, 121–135 (2018).
78. Braconnot, P. & Marti, O. Impact of precession on monsoon characteristics from coupled ocean atmosphere experiments: changes in Indian monsoon and Indian ocean climatology. *Mar. Geol.* **201**, 23–34 (2003).
79. Prescott, C., Haywood, A., Dolan, A., Hunter, S. & Tindall, J. Indian monsoon variability in response to orbital forcing during the late Pliocene. *Glob. Planet. Change* **173**, 33–46 (2019).
80. Erb, M. P. et al. Response of the equatorial pacific seasonal cycle to orbital forcing. *J. Clim.* **28**, 9258–9276 (2015).
81. Chen, M.-T. & Beaufort, L. Exploring quaternary variability of the east Asia monsoon, Kuroshio Current, and western Pacific warm pool systems: high-resolution investigations of paleoceanography from the IMAGES III (MD106) IPHIS cruise. *Terr. Atmos. Ocean. Sci.* **9**, 129–142 (1998).
82. Gartner, S. Paleoceanography of the mid-Pleistocene. *Mar. Micropaleont.* **13**, 23–46 (1988).
83. Pujo, A. & Giradeau, J. Distribution of Noelaerhabdaceae (calcareous nannofossils) in the upper and middle Quaternary of the Atlantic and Pacific oceans. *Oceanolog. Acta* **16**, 349–362 (1993).

**Acknowledgements** This paper is a contribution of the Climate research group at CEREGE. This research uses samples provided by the IODP. We thank the scientists, technical staff and crews of IODP expeditions 353 and 363 and IMAGES expeditions 3 and 13; A. Fruy and S. Sergi for sample preparation assistance; and the CEA–CCRT for providing access to the HPC resources of TGCC under the allocation 2019-A0070102212 made by GENCI. We acknowledge French ANR projects CALHIS (L.B.), iMonsoon (C.T.B.) and AMOR (Y.D.), and INSU project CALVE (C.T.B.) and FRB project COCCACE (L.B.), which provided funding for this work. IODP France provided post-cruise funding to L.B. and C.T.B.

**Author contributions** L.B. designed the study. L.B., Y.G., N.B. and M.T. developed automated artificial intelligence methods. L.B., C.T.B., J.-C.M., P.C., E.G. and S.B. prepared samples and/or generated data. A.-C.S. designed and ran the model simulations, in collaboration with Y.D. L.B. and C.T.B. analysed the morphometric data. L.B., C.T.B., A.-C.S., B.S.-M., Y.D. and Y.R. discussed

interpretations. L.B., C.T.B. and A.-C.S. wrote the manuscript with contributions from B.S.-M., Y.D. and Y.R.

**Competing interests** The authors declare no competing interests.

**Additional information**

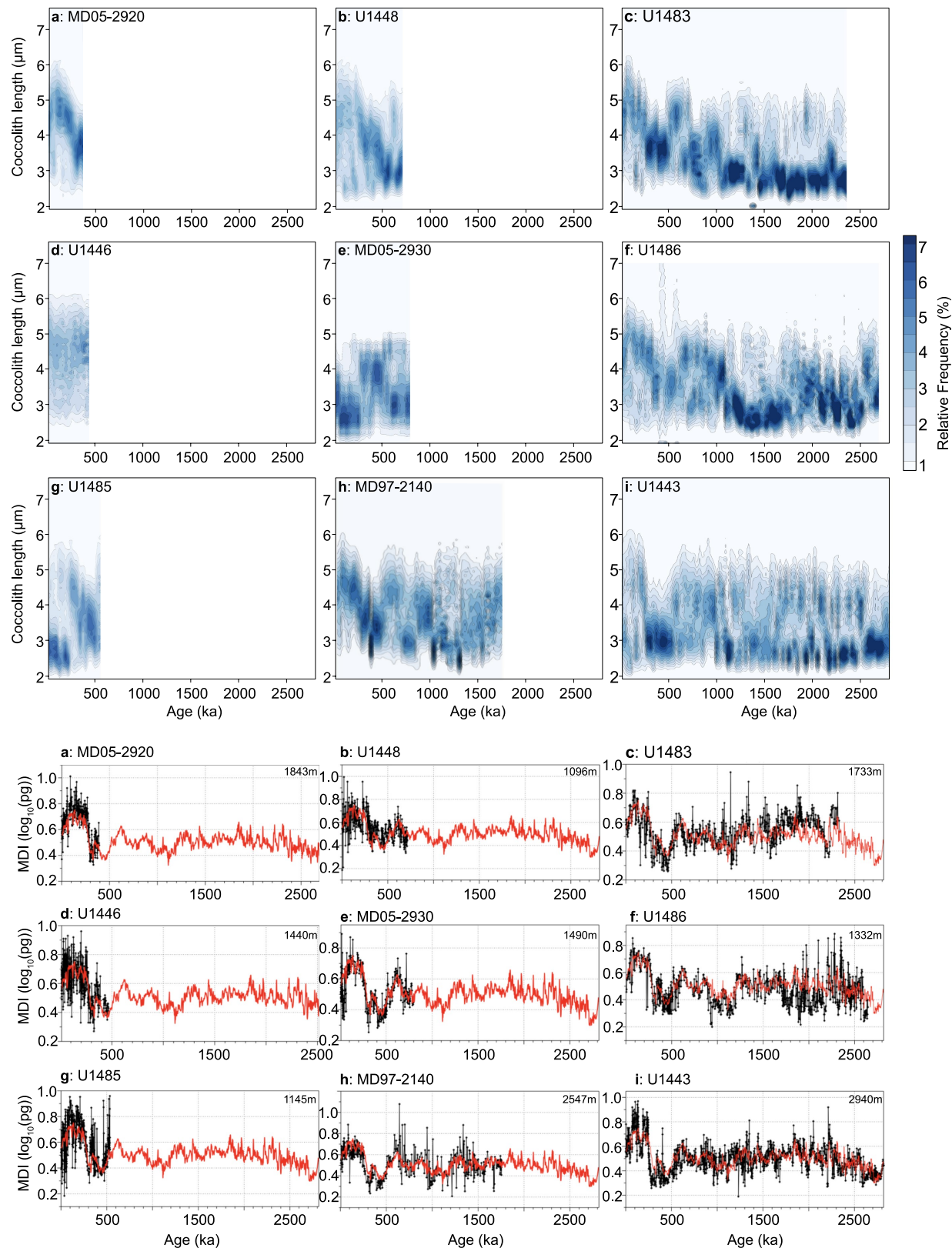
**Supplementary information** The online version contains supplementary material available at <https://doi.org/10.1038/s41586-021-04195-7>.

**Correspondence and requests for materials** should be addressed to Luc Beaufort or Clara T. Bolton.

**Peer review information** *Nature* thanks Claudia Agnini, Ying Guan, Rosalind Rickaby, Andy Ridgwell and Thomas Westerhold for their contribution to the peer review of this work. Peer reviewer reports are available.

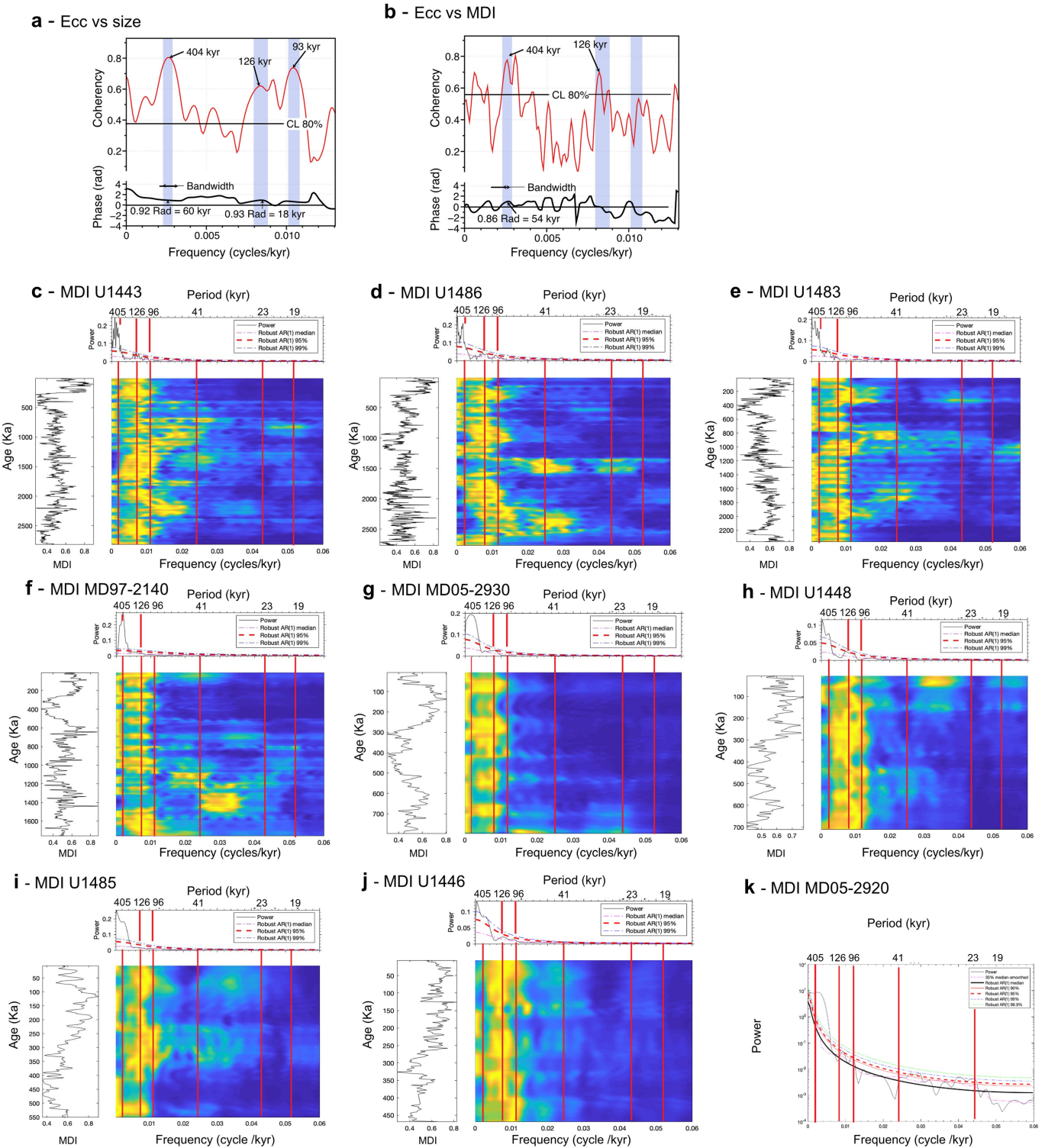
**Reprints and permissions information** is available at <http://www.nature.com/reprints>.

# Article



**Extended Data Fig. 1 | Size and MDI records for each core.** Top panels **a** to **i**: Size frequency plots for each individual core used to create the composite record shown in Fig. 1a. Bottom panels **a** to **i**: Individual MDI records for each

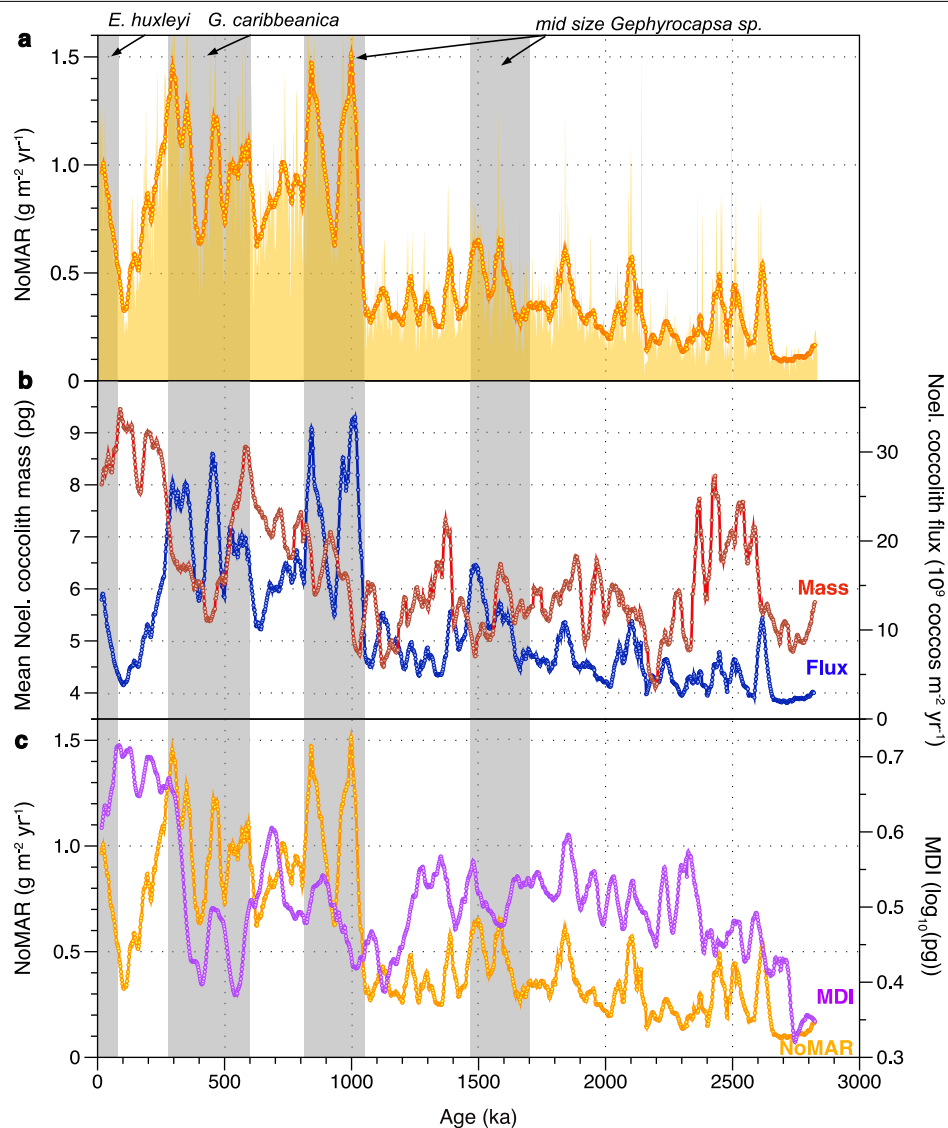
core (black lines and points) plotted with the stacked MDI record (red line). Pearson correlation coefficients between individual sites and the stack vary between 0.71 and 0.93 (*P* values are all  $<0.00001$ ).



#### Extended Data Fig. 2 | Time-series analyses of individual records.

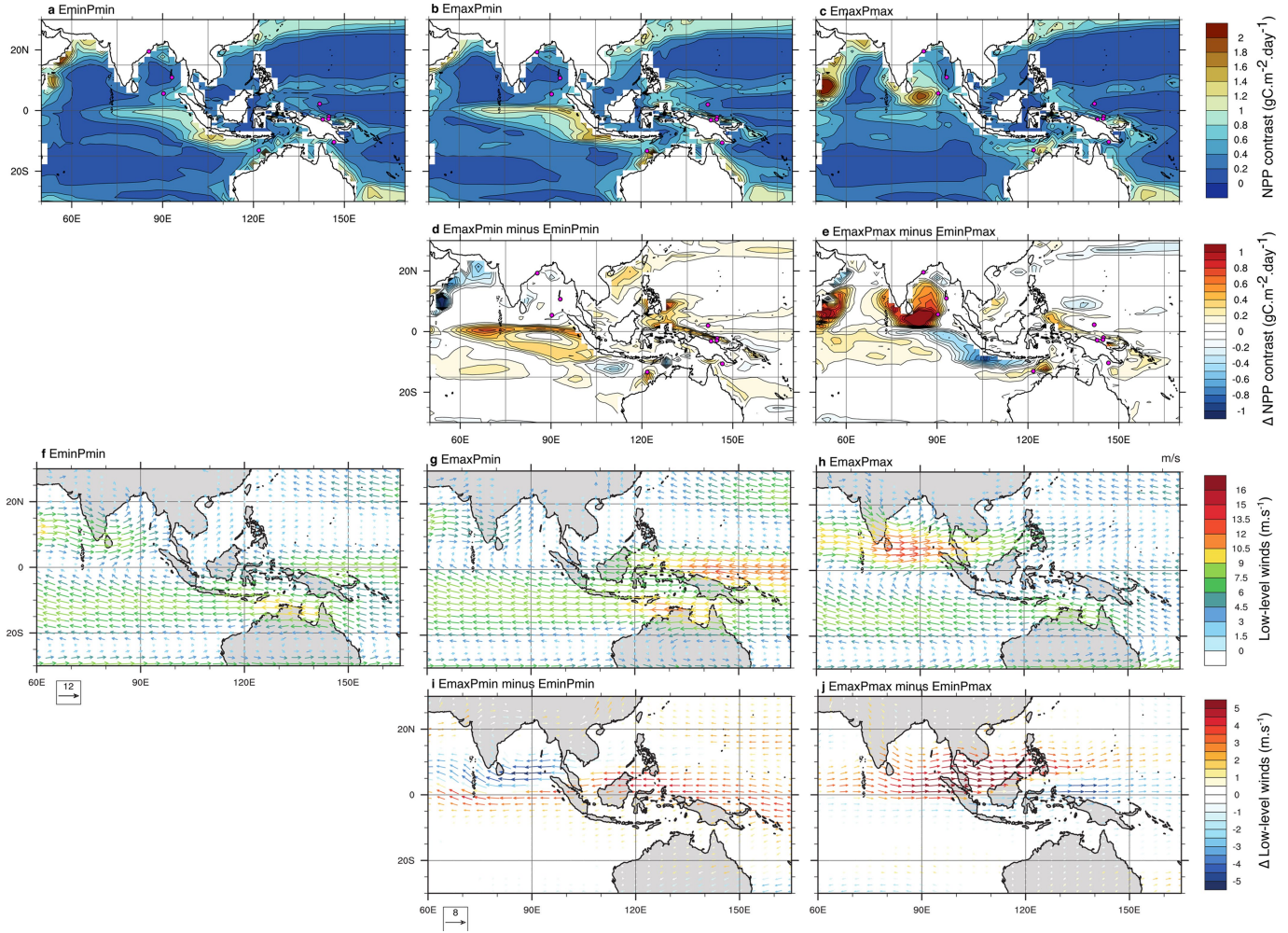
**a, b**, Blackman Tukey cross-spectral analysis between eccentricity and stacked coccolith length (**a**) and eccentricity and stacked MDI (**b**). Top: coherency; Bottom: phase (radian).

(see Methods) of detrended individual MDI series resampled at 2-kyr intervals (shown on left of each evolutive analysis). Primary orbital periods are shown by red lines.



**Extended Data Fig. 3 | Decomposition of the Noelaerhabdaceae mass accumulation rate (NoMAR) record into its mass and flux components.**  
**a**, Stacked NoMAR record, binned into 2-ky intervals (orange shading) and smoothed with a 30-kyr moving window (orange line), **b**, Noelaerhabdaceae coccolith flux (blue) and average Noelaerhabdaceae coccolith mass (red).

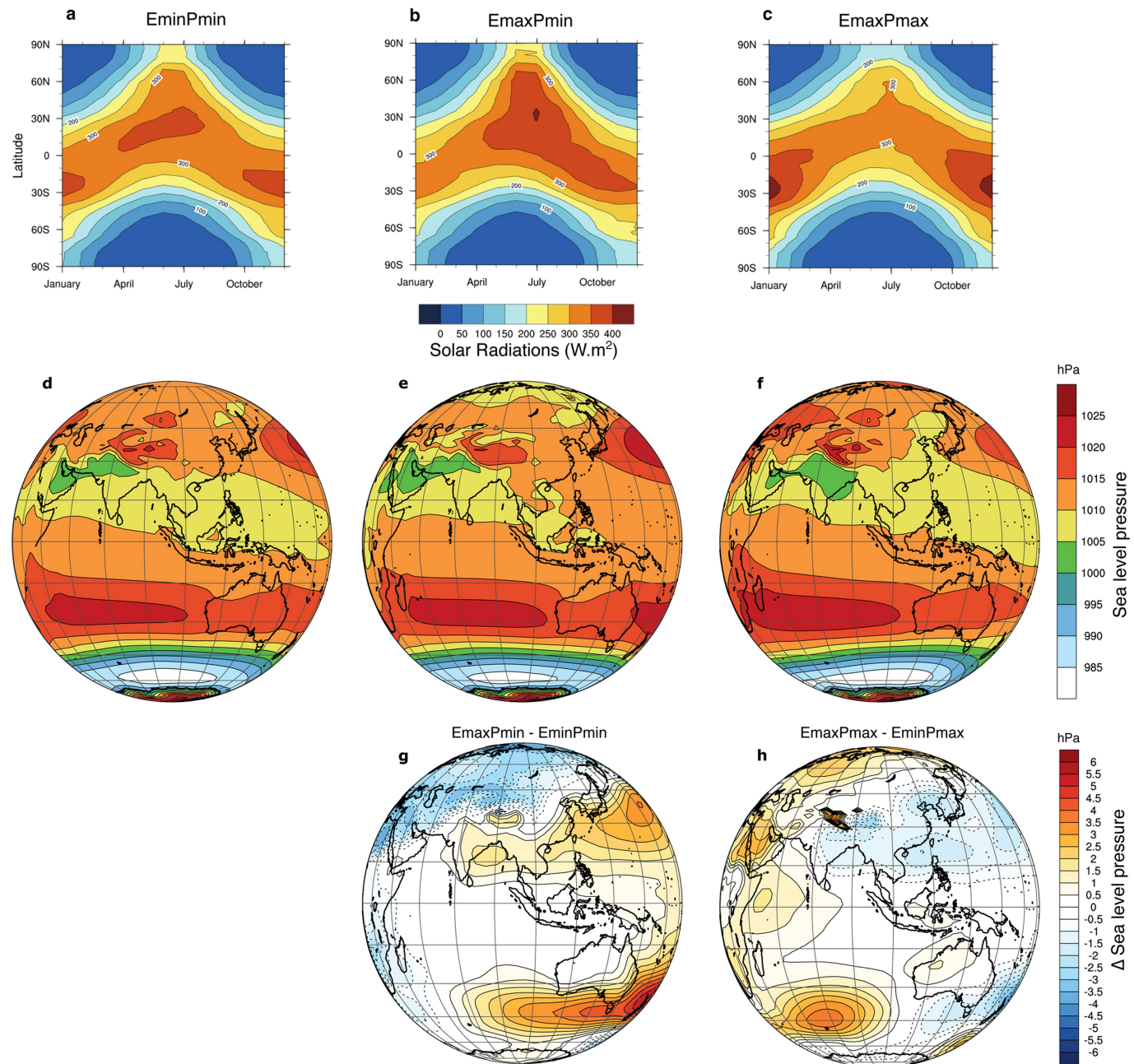
Here, stacked mass and flux records are smoothed with a 30-kyr moving window as in **a**. **c**, NoMAR (orange) and MDI (purple) records, smoothed with a 30-kyr moving window. Grey shaded areas represent four described acmes of mid-size Noelaerhabdaceae species<sup>19–21,82,83</sup>.



**Extended Data Fig. 4 | Ocean–atmosphere model outputs under different orbital configurations.** Top: Yearly maximum contrast in NPP ( $\text{gC m}^{-2} \text{day}^{-1}$ ) for **a**:  $E_{\min} P_{\min}$ , **b**:  $E_{\max} P_{\min}$  and **c**:  $E_{\max} P_{\max}$ . Low eccentricity values minimize the amplitude of precession variability, thus we only show results for minimum precession value at minimum eccentricity ( $E_{\min} P_{\min}$ ) but the reader can consider those results to be similar for the  $E_{\min} P_{\max}$  simulation. **d** and **e** represent the anomaly of yearly maximum contrast in NPP. At  $E_{\max} P_{\max}$ , the eastern equatorial Indian Ocean exhibits moderate seasonality (**a**) due to inhibition of the summer

productivity induced by lower nutrient concentrations in this area (Extended Data Fig. 6a). In this case, high productivity areas during boreal summer are shifted to south-west of India. Bottom: Late summer (JASO) low-level winds for **f**:  $E_{\min} P_{\min}$ , **g**:  $E_{\max} P_{\min}$ , **h**:  $E_{\max} P_{\max}$  simulations. **i** and **j** represent the anomaly in late summer low-level winds. At  $E_{\max} P_{\max}$  the north-equatorial westerlies (**c**, **e**) are confined to south of  $10^{\circ}$  N owing to the extension above India of the low-pressure area.

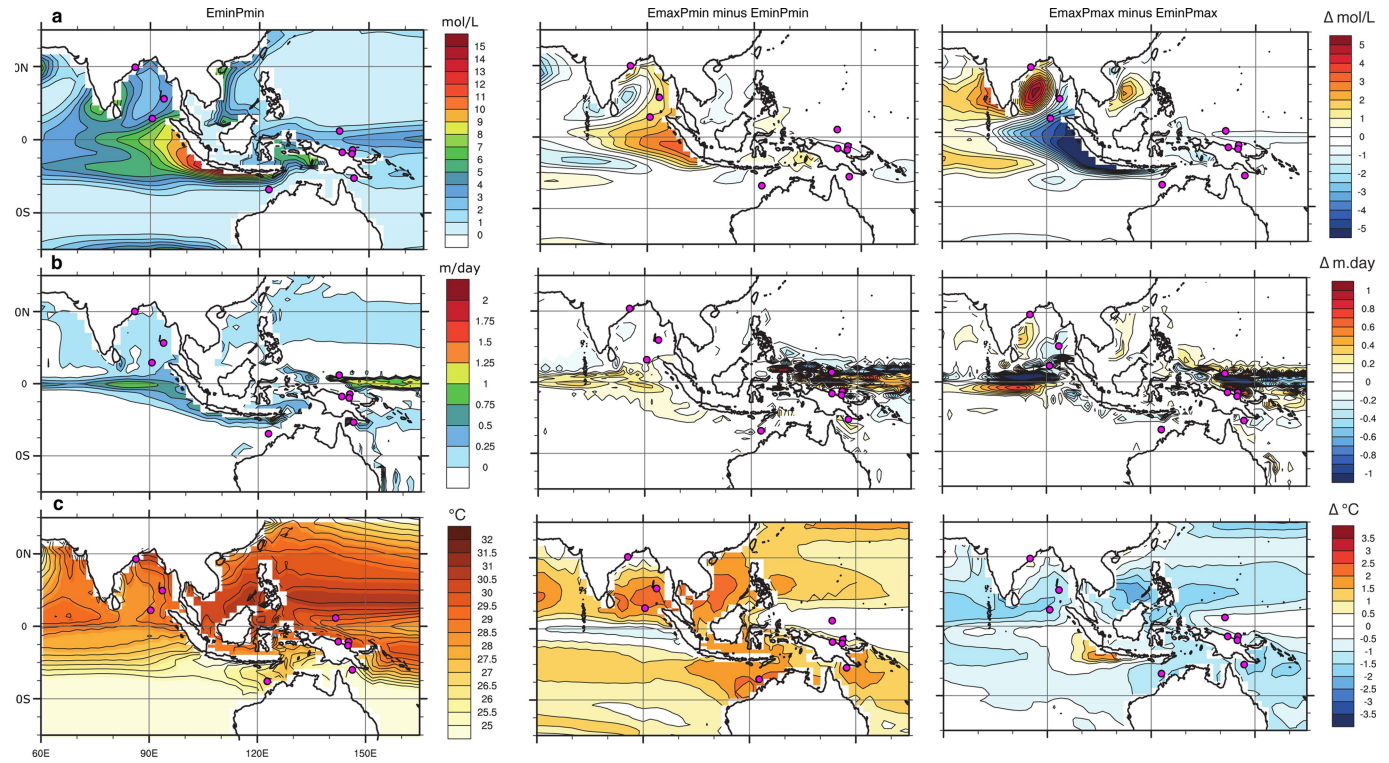
# Article



## Extended Data Fig. 5 | Solar radiation and sea-level pressure in model

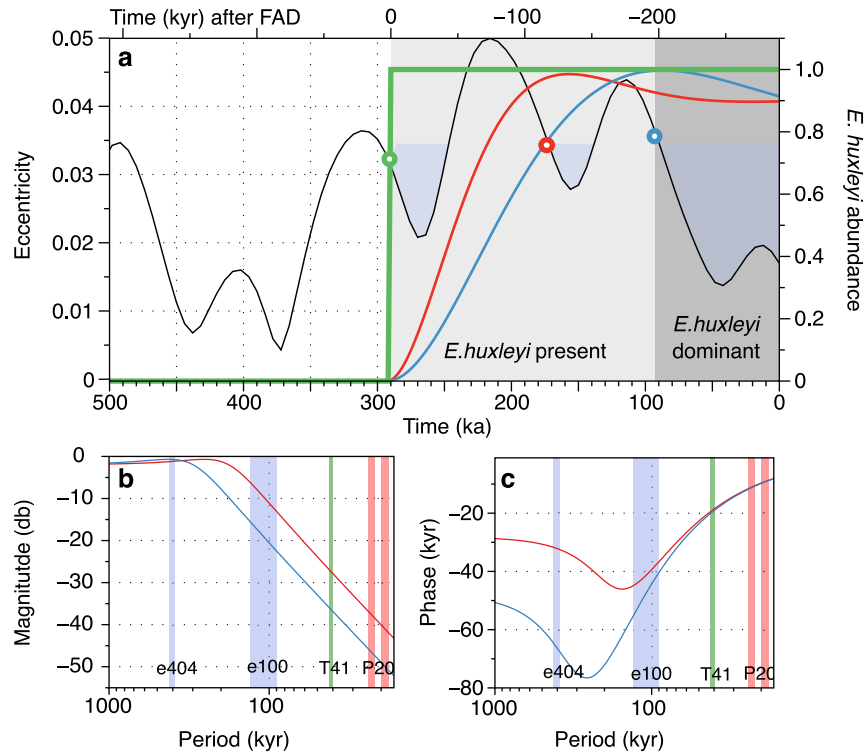
**simulations.** Seasonal latitudinal variations of solar radiation at the top of the atmosphere derived from the model ( $\text{W} \cdot \text{m}^{-2}$ ); **a:**  $E_{\min} P_{\min}$ , **b:**  $E_{\max} P_{\min}$ , **c:**  $E_{\max} P_{\max}$ . See Extended Data Table 3 for details of orbital configurations of each

simulation. Late summer (JASO) low-level winds for **d:**  $E_{\min} P_{\min}$ , **e:**  $E_{\max} P_{\min}$ , **f:**  $E_{\max} P_{\max}$  simulations and anomaly in late summer low-level winds, **g:**  $E_{\max} P_{\min}$  minus  $E_{\min} P_{\min}$ , **h:**  $E_{\max} P_{\max}$  minus  $E_{\min} P_{\max}$ .



**Extended Data Fig. 6 | Nutrients, temperature and upwelling in model simulations.** **a**,  $\text{NO}_3$  concentrations in the surface layer (0–100 m). **b**, Upwelling velocity (averaged between 40 and 80 m). **c**, Sea Surface Temperature (SST). All

variables are averaged over JASO. Left:  $E_{\min}$ ; Middle:  $E_{\max}P_{\min}$  minus  $E_{\min}P_{\min}$ ; Right:  $E_{\max}P_{\max}$  minus  $E_{\min}P_{\max}$ .



**Extended Data Fig. 7 | Explanation of non-linearities in coccolithophore evolution.** **a**, Low-pass filter design for the delay between first appearance datum (FAD) and the beginning of the acme (BA) for *E. huxleyi* (blue line, lag of two eccentricity cycles) and another possible scenario for another species (red line, lag of one eccentricity cycle). The stepped green line represents *E. huxleyi*'s existence (0 = absence, 1 = presence). The blue and red curves in all

panels are the output series of the 2 low-pass filters described in the Methods. The black curve in **a** represents coeval eccentricity values. **b, c**, Bode plots of the 1-cycle lag filter (red) and the 2-cycle lag filter (blue) for magnitude (**b**) and phase (**c**) (see Methods). Earth's primary orbital periods are indicated by shading.

**Extended Data Table 1 | Characteristics of the nine marine records used in this study**

Site Name	Expedition	Longitude	Latitude	Water Depth (m)	Biome	Record length (kyr)	Mean Resolution (kyr)	Number of samples	Number of Measurements
U1446	IODP 353	85°441	19°050 N	1440	INDE	468	0.5	952	222119
U1448	IODP 353	93°00.00	10°38.03 N	1096	MONS	716	1.1	624	617138
U1443	IODP 353	90°21.71	5°23.01 N	2940	MONS	2818	1.6	1717	1337793
MD97-2140	IMAGES 3	141°45.49	2°02.59 N	2547	WARM	1758	1.4	1241	540523
U1486	IODP 363	144°36.08	2°22.34 S	1332	WARM	2661	2.2	1195	1004860
MD05-2920	IMAGES 13	144°32	2°51.48 S	1843	WARM	387	1.1	353	436984
U1485	IODP 363	142°47.59	3°06.16 S	1145	SUND	535	0.9	587	580612
MD05-2930	IMAGES 13	146°15.73	10°25.30 S	1490	AUSE	793	2.1	372	620736
U1483	IODP 363	121°5.24	13°05.24 S	1733	ISSG	2332	2.3	994	1777406

**Mean = 1.6      Sum = 8035      Sum = 7138171**

Biome codes follow reference 25: INDE, Eastern India Coastal province; MONS, Indian Monsoon Gyres Province; WARM, Western Pacific Warm Pool province; SUND, Sunda-Arafura Shelves Province; AUSE, East Australian Coastal Province; ISSG, Indian South Subtropical Gyre Province. These cores were retrieved during four expeditions: IMAGES expeditions 3 (ref. <sup>81</sup>) and 13 (ref. <sup>50</sup>), and IODP expeditions 353 (ref. <sup>53</sup>) and 363 (ref. <sup>58</sup>), which took place in the Western Pacific and Indian tropical oceans (Fig. 3a).

# Article

**Extended Data Table 2 | Relative calcium carbonate mass contribution per calcareous nannofossil taxon or group for each sediment core**

Order/Family/genus	Average all sites (%)	U1483 (%)	MD97-2140 (%)	U1486 (%)	U1485 (%)	MD05-2920 (%)	U1443 (%)	U1446 (%)	U1448 (%)
Noelaerhabdaceae	49	53	59	54	45	61	36	27	54
Coccolithales	3	2	5	2	2	3	4	4	4
Zygodiscales + Syracosphaerales	16	19	16	7	9	16	23	20	14
Florisphaera	30	23	14	37	42	18	37	48	25
Others	2	2	6	1	2	2	1	1	4

In each case, values represent the average of the entire time series. Values were calculated by multiplying the number of individuals recognized for each taxon (class<sup>42</sup> grouped by taxon : Noelaerhabdaceae (*Emiliania*, *Gephyrocapsa*, *Pseudoemiliania* and *Reticulofenestra*), Coccolithales (*Calcidiscus*, *Coccolithus* and *Umbellicosphaera*), and Helicosphaerales + Syracosphaerales (*Helicosphaera*, *Pontosphaera*, *Syracosphaera* and *Rhabdolithus*)) multiplied by the averaged mass of the considered class in that core. This calculation was not possible for core MD05-2930 as some species abundance data were not available.

**Extended Data Table 3 | Summary of orbital parameters<sup>23</sup> used for each simulation and mean yearly contrast of radiation at equator (Wm<sup>-2</sup>) derived from IPSL-CM5A2**

Configuration (kyr)	Eccentricity	Precession	Longitude of perihelion (°)	Obliquity (°)	Mean YCR at Equator (W.m <sup>-2</sup> )
C2222 (EmaxPmax)	0.054	0.054	87	23.73	74
C2230 (EmaxPmin)	0.053	-0.037	315	23.84	83
C2265	0.026	0.024	115	24.28	59
C2346	0.034	-0.033	287	24.27	62
C2369	0.016	-0.015	256	22.26	52
C2380 (EminPmax)	0.006	0.006	77	23.74	37
C2395 (EminPmin)	0.005	-0.003	310	23.42	39

See Methods for further information.

## Reporting Summary

Nature Portfolio wishes to improve the reproducibility of the work that we publish. This form provides structure for consistency and transparency in reporting. For further information on Nature Portfolio policies, see our [Editorial Policies](#) and the [Editorial Policy Checklist](#).

### Statistics

For all statistical analyses, confirm that the following items are present in the figure legend, table legend, main text, or Methods section.

n/a Confirmed

- The exact sample size ( $n$ ) for each experimental group/condition, given as a discrete number and unit of measurement
- A statement on whether measurements were taken from distinct samples or whether the same sample was measured repeatedly
- The statistical test(s) used AND whether they are one- or two-sided  
*Only common tests should be described solely by name; describe more complex techniques in the Methods section.*
- A description of all covariates tested
- A description of any assumptions or corrections, such as tests of normality and adjustment for multiple comparisons
- A full description of the statistical parameters including central tendency (e.g. means) or other basic estimates (e.g. regression coefficient) AND variation (e.g. standard deviation) or associated estimates of uncertainty (e.g. confidence intervals)
- For null hypothesis testing, the test statistic (e.g.  $F$ ,  $t$ ,  $r$ ) with confidence intervals, effect sizes, degrees of freedom and  $P$  value noted  
*Give  $P$  values as exact values whenever suitable.*
- For Bayesian analysis, information on the choice of priors and Markov chain Monte Carlo settings
- For hierarchical and complex designs, identification of the appropriate level for tests and full reporting of outcomes
- Estimates of effect sizes (e.g. Cohen's  $d$ , Pearson's  $r$ ), indicating how they were calculated

*Our web collection on [statistics for biologists](#) contains articles on many of the points above.*

### Software and code

Policy information about [availability of computer code](#)

Data collection	The data collection was done with SYRACO III (version 2015), a custom algorithm first published in 1998. The description of this algorithm is provided in the Methods.
Data analysis	Time series analysis were performed with the following software packages : 1) Analyses 2.0.8: (Paillard, D., Labeyrie, L. & Yiou, P. Macintosh program performs time-series analysis. Eos Trans. AGU, 77, 379 (1996)) 2) Acycle 2.2 (Li, M., Hinnov, L. & Kump, L. Acycle: Time-series analysis software for paleoclimate research and education. Computers & Geosciences 127, 12-22, doi: <a href="https://doi.org/10.1016/j.cageo.2019.02.011">https://doi.org/10.1016/j.cageo.2019.02.011</a> (2019)).

For manuscripts utilizing custom algorithms or software that are central to the research but not yet described in published literature, software must be made available to editors and reviewers. We strongly encourage code deposition in a community repository (e.g. GitHub). See the Nature Portfolio [guidelines for submitting code & software](#) for further information.

### Data

Policy information about [availability of data](#)

All manuscripts must include a [data availability statement](#). This statement should provide the following information, where applicable:

- Accession codes, unique identifiers, or web links for publicly available datasets
- A description of any restrictions on data availability
- For clinical datasets or third party data, please ensure that the statement adheres to our [policy](#)

All coccolith morphological data, as well as all model outputs described in the paper (including NPP and main oceanic and atmospheric variables) are archived at the French oceanographic data repository SEANOE at <https://doi.org/10.17882/84031>

# Field-specific reporting

Please select the one below that is the best fit for your research. If you are not sure, read the appropriate sections before making your selection.

- Life sciences       Behavioural & social sciences       Ecological, evolutionary & environmental sciences

For a reference copy of the document with all sections, see [nature.com/documents/nr-reporting-summary-flat.pdf](https://nature.com/documents/nr-reporting-summary-flat.pdf)

## Ecological, evolutionary & environmental sciences study design

All studies must disclose on these points even when the disclosure is negative.

Study description

A paleoecological and evolutionary study based on marine sedimentary records. Morphological parameters of fossil remains of calcifying plankton are based on simple description (size and mass) resulting from microscope analysis of a large number of samples.

Research sample

Specimens of Noelaerhabdaceae (the most abundant group of coccolithophores in the tropics during the Pleistocene) were studied in samples from nine different Indo-Pacific sediment cores. The study covers the Pleistocene. Those core were chosen for this study because they cover a wide geographical area and belong to different oceanic biomes, they are well dated, they have sufficient sedimentation rates to allow good time resolution (about two thousand year), and because the coccoliths are well preserved.

Sampling strategy

Core retrieval was carried out by two research vessels (R/V Marion-Dufresne and R/V Joides Resolution) during 4 oceanographic expeditions, at locations carefully chosen by chief scientists in places where the sediment was expected to be of excellent quality (i.e., recording continuous well-preserved sediment sequences). The R/V Joides Resolution is a riserless drilling ship that uses Hydraulic Piston coring. The R/V Marion-Dufresne is a research ship that uses technology capable of recovering the longest piston cores available (CALYPSO giant piston corer), and routinely recovers sediment cores longer than 30 m.

Data collection

Each core was sampled at 10 cm or 20 cm intervals (depending on the sedimentation rate). About 2cc of sediment were collected. A small amount of each sample was diluted and homogenized in water. The suspended sediment was then decanted onto a cover slip and mounted onto a microscope slide for analysis. Each sample contains a huge number of fossil coccoliths (>1000000/cc)

Timing and spatial scale

The data generated in this study cover the Pleistocene (last 2.6 Ma) with an average resolution of 1600 years. The spatial scale covers the tropics in the western Pacific Ocean and the eastern Indian Ocean.

Data exclusions

No data exclusion

Reproducibility

Reproducibility is achieved by the high number of coccoliths measured in each sample (usually at least 1000), by the high number of total samples (8035), and by the high resolution of the records (~2000 years) that far exceeds the targeted climate cycles (>80000 years), and by using nine different cores from different oceanographic biomes.

Randomization

Not applicable : Randomization is embedded in our sampling process which does not target specific ages, and used a random portion (about 1000 individuals) of an extremely large population of coccoliths in each sample (several million).

Blinding

Not applicable : Blinding is embedded in our methodology since it is entirely automated and the counting and the measurements are carried out by computer without human control.

Did the study involve field work?  Yes  No

## Field work, collection and transport

Field conditions

Not relevant : geological samples obtained by coring or drilling are not dependent on modern weather conditions. The cores are processed and stored rapidly, placed at 5°C and are therefore stabilized. The coccoliths within the sediment cores are usually not affected by field and storage conditions.

Location

Site/ Expedition / Longitude / Latitude / Water Depth (m)  
 IODP U1446 / IODP 353 / 85°44'1 / 19°05'0 N / 1440 m  
 IODP U1448 / IODP 353 / 93°00'0.00 / 10°38.03 N / 1096 m  
 IODP U1443 / ODP 353 / 90°21.71'5"23.01 N / 2940 m  
 IMAGES MD97-2140 / IMAGES 3 / 141°45.49 / 2°02.59 N / 2547 m  
 IODP U1486 / IODP 363 / 144°36.08 / 2°22.34 S / 1332 m  
 IMAGES MD05-2920 / IMAGES 13 / 144°32 / 2°51.48 S / 1843 m  
 IODP U1485 / IODP 363 / 142°47.59 / 3°06.16 S / 1145 m  
 IMAGES MD05-2930 / IMAGES 13 / 146°15.73 / 10°25.30 S / 1490 m  
 IODP U1483 / IODP 363 / 121°5.24 / 13°05.24 S / 1733 m

Access & import/export

Not relevant: All coring was carried out with the required permissions

Disturbance

Not relevant: retrieving deep sea cores does not disturb deep sea environment

# Reporting for specific materials, systems and methods

We require information from authors about some types of materials, experimental systems and methods used in many studies. Here, indicate whether each material, system or method listed is relevant to your study. If you are not sure if a list item applies to your research, read the appropriate section before selecting a response.

## Materials & experimental systems

n/a	<input type="checkbox"/> Involved in the study <input checked="" type="checkbox"/> Antibodies <input checked="" type="checkbox"/> Eukaryotic cell lines <input type="checkbox"/> Palaeontology and archaeology <input checked="" type="checkbox"/> Animals and other organisms <input checked="" type="checkbox"/> Human research participants <input checked="" type="checkbox"/> Clinical data <input checked="" type="checkbox"/> Dual use research of concern
-----	--

## Methods

n/a	<input type="checkbox"/> Involved in the study <input checked="" type="checkbox"/> ChIP-seq <input checked="" type="checkbox"/> Flow cytometry <input checked="" type="checkbox"/> MRI-based neuroimaging
-----	--

## Palaeontology and Archaeology

### Specimen provenance

All four international coring expeditions received working permits from the concerned countries when sampling took place in territorial waters, including from Papua New Guinea in 2005 to the Institut Polaire Paul Emile Victor and in 2017 to IODP, from Australia in 2017 to IODP, and from India in 2014–2015 to IODP.

### Specimen deposition

Original samples and microscope slides containing the analysed samples are stored at CEREGE (Aix en Provence, France) and are available.

### Dating methods

The core chronologies are published in other papers, and no new dates were provided in this paper. See Methods for details.

Tick this box to confirm that the raw and calibrated dates are available in the paper or in Supplementary Information.

### Ethics oversight

No ethical approval was required for this study as it concerns microfossils.

Note that full information on the approval of the study protocol must also be provided in the manuscript.